The Role of Subtropical Rossby Waves in Amplifying the Divergent Circulation of the Madden–Julian Oscillation

PRAGALLVA BARPANDA,[a,b] STEFAN N. TULICH,[a,b] JULIANA DIAS,[b] AND GEORGE N. KILADIS[b]

[a] *Cooperative Institute for Research in Environmental Sciences, University of Colorado Boulder, Boulder, Colorado*
[b] *NOAA/Physical Sciences Laboratory, Boulder, Colorado*

(Manuscript received 14 December 2022, in final form 21 June 2023, accepted 11 July 2023)

ABSTRACT: The composite structure of the Madden–Julian oscillation (MJO) has long been known to feature pronounced Rossby gyres in the subtropical upper troposphere, whose existence can be interpreted as the forced response to convective heating anomalies in the presence of a subtropical westerly jet. The question of interest here is whether these forced gyre circulations have any subsequent effects on divergence patterns in the tropics and the Kelvin-mode component of the MJO. A nonlinear spherical shallow water model is used to investigate how the introduction of different background jet profiles affects the model's steady-state response to an imposed MJO-like stationary thermal forcing. Results show that a stronger jet leads to a stronger Kelvin-mode response in the tropics up to a critical jet speed, along with stronger divergence anomalies in the vicinity of the forcing. To understand this behavior, additional calculations are performed in which a localized vorticity forcing is imposed in the extratropics, without any thermal forcing in the tropics. The response is once again seen to include pronounced equatorial Kelvin waves, provided the jet is of sufficient amplitude. A detailed analysis of the vorticity budget reveals that the zonal-mean zonal wind shear plays a key role in amplifying the Kelvin-mode divergent winds near the equator, with the effects of nonlinearities being of negligible importance. These results help to explain why the MJO tends to be strongest during boreal winter when the Indo-Pacific jet is typically at its strongest.

SIGNIFICANCE STATEMENT: The MJO is a planetary-scale convectively coupled equatorial disturbance that serves as a primary source of atmospheric predictability on intraseasonal time scales (30–90 days). Due to its dominance and spontaneous recurrence, the MJO has a significant global impact, influencing hurricanes in the tropics, storm tracks, and atmosphere blocking events in the midlatitudes, and even weather systems near the poles. Despite steady improvements in subseasonal-to-seasonal (S2S) forecast models, the MJO prediction skill has still not reached its maximum potential. The root of this challenge is partly due to our lack of understanding of how the MJO interacts with the background mean flow. In this work, we use a simple one-layer atmospheric model with idealized heating and vorticity sources to understand the impact of the subtropical jet on the MJO amplitude and its horizontal structure.

KEYWORDS: Kelvin waves; Rossby waves; Shallow-water equations; Wind shear; Madden-Julian oscillation; Upper troposphere

1. Introduction

The Madden–Julian oscillation (MJO) is a planetary-scale equatorial disturbance that dominates tropical variability on intraseasonal time scales. The disturbance is typified by a zonal dipole pattern in convective heating and cooling that moves eastward at a phase speed of ~5 m s^{-1}. The heating and cooling extends through the depth of the troposphere and drives horizontal divergence and convergence at upper levels (~200 hPa) and convergence and divergence below, respectively (Kiladis et al. 2005, and references therein). The upper-tropospheric component of the MJO's circulation has a much larger meridional extent than its lower-tropospheric component and is marked by pronounced off-equatorial cyclonic and anticyclonic Rossby gyres whose centers lie in the subtropics (Knutson and Weickmann 1987; Rui and Wang 1990; Kiladis and Weickmann 1992; Hendon and Salby 1994; Kiladis et al. 2005).

The Rossby gyres are thought to be a result of interaction between the convectively forced divergent flow with the basic-state vorticity gradient, known as the "Rossby wave source" (Sardeshmukh and Hoskins 1988). Wintertime MJO composites reveal that these gyres form on the southern flank of the subtropical westerly jet, move eastward in tandem with the MJO convection, and are most pronounced in the Indo-Pacific sector—a region where both MJO convective activity and the subtropical jet are found to be the strongest in the boreal winter (Adames and Wallace 2014). The relative location of the MJO-induced Rossby gyres with respect to the climatological background flow affects extratropical teleconnection patterns that influence global weather on subseasonal-to-seasonal time scales (Liebmann and Hartmann 1984; Weickmann et al. 1985; Lau and Lau 1986; Lau and Phillips 1986; Knutson and Weickmann 1987; Ferranti et al. 1990; Hoskins and Ambrizzi 1993; Jin and Hoskins 1995; Hsu 1996; Matthews et al. 2004; Lin et al. 2010; Seo and Lee 2017; Tseng et al. 2019; Hall et al. 2020).

Supplemental information related to this paper is available at the Journals Online website: https://doi.org/10.1175/JAS-D-22-0259.s1.

Corresponding author: Pragallva Barpanda, pragallva.barpanda@uib.no

DOI: 10.1175/JAS-D-22-0259.1

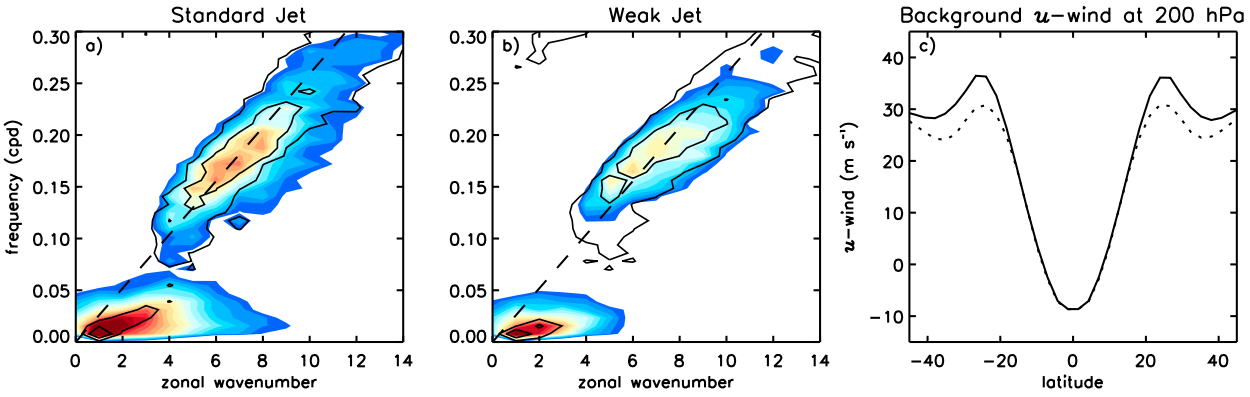

FIG. 1. Tropical rain spectra from TK21 for (a) standard IPAC and (b) weak IPAC jet experiments. (c) Comparison of zonal-mean zonal wind profiles at 200 hPa for standard IPAC (solid curve) and weak IPAC (dashed curve) cases. See their Table 1 for experimental details.

However, the connection between the MJO and extratropics is not just in one direction.

There have been several different studies indicating that extratropical variability has an important influence on the MJO. Among the earliest is the study by Straus and Lindzen (2000), who documented a strong coherence between slow eastward-propagating circulation signals in the subtropical upper troposphere and the MJO zonal winds in the tropics. Although they attributed the subtropical low-frequency variability to planetary-scale baroclinic instability (Frederiksen and Frederiksen 1997), the baroclinic generation of extratropical long waves is not well understood, and remains an active area of research (Hsieh et al. 2021; Moon et al. 2022). On the modeling side, Lin et al. (2007) used a dry atmospheric model with a wintertime basic state and showed that an MJO-like disturbance (in the form of a slow planetary-scale Kelvin wave with 15 m s^{-1} phase speed) can be generated in the Eastern Hemisphere in response to an imposed subtropical forcing. Ray and Zhang (2010) also performed experiments using a tropical channel model and were able to initiate an MJO event by including extratropical influences via lateral boundary conditions. Subsequently, Ray and Li (2013) performed mechanism denial experiments and showed that they could eliminate the MJO by suppressing extratropical waves. A potential issue with that study, however, was later identified by Ma and Kuang (2016), who performed more carefully designed experiments showing that the MJO "can exist without extratropical influence," provided the basic state is maintained. At the same time, there are some competing MJO theories based on the dynamics of Rossby vortices that implicitly include extratropical influences on the MJO (Yano and Tribbia 2017; Rostami and Zeitlin 2019; Hayashi and Itoh 2017).

Such disparate findings and viewpoints are reflective of our general lack of understanding of how extratropical circulations interact with the MJO. Nevertheless, there is broad agreement that the subtropical jet and attendant Rossby gyres are important for providing a complete dynamical description of the phenomenon. While many studies have primarily focused on the forcing of subtropical circulations by the MJO (Schwendike et al. 2021, and references therein), here we focus on the opposite side of the coin, namely, how does the presence and strength of a subtropical jet affect the MJO?

Recently Tulich and Kiladis (2021, hereafter TK21) explored the impact of jet structure on the MJO and convectively coupled Kelvin waves in aquaplanet experiments performed using the superparameterized Weather Research and Forecasting Model (SP-WRF). They prescribed zonally symmetric sea surface temperature and nudged the subtropics toward a desired wind profile and found considerable weakening of the MJO signal when the model's Indo-Pacific (IPAC) subtropical jet was weakened by 25% (Fig. 1; see TK21 for details). Although the sophisticated SP-WRF modeling setup produced a reasonably realistic MJO, the model complexity masked the precise pathway by which the jet controlled the simulated MJO strength.

To disentangle the feedback mechanism from the subtropics to the tropics, here we use a dry spherical shallow water model with variable jet speeds and perform two types of forcing experiments, namely, MJO-like thermal forcing at the equator and MJO induced gyre-like vorticity forcing in the subtropics. We then use a steady-state vorticity budget to show how the Rossby mode generated by each type of forcing experiments influences the Kelvin-mode divergence as a function of subtropical jet speed.

The paper is organized as follows. In section 2, we provide model details and outline the analytical approach for decomposing the model divergence into Matsuno–Gill modes and dynamical quantities from the vorticity budget. Section 3 describes the results of the steady-state model response for different jet speeds in response to thermal forcing and vorticity forcing experiments. Finally, in section 4 we discuss and summarize our results.

2. Methods

a. Model setup

We use a nonlinear spherical shallow water model to investigate how the structure of the background flow affects the atmosphere's response to an imposed MJO-like forcing, in the

absence of moisture effects.[1] The model setup is similar to that of Kraucunas and Hartmann (2007) and Monteiro et al. (2014). Briefly, the model solves for relative vorticity (ζ), divergence (D), and geopotential (ϕ) in spherical coordinates specified by latitude (θ) and longitude (λ). The complete set of equations is

$$\frac{\partial \zeta}{\partial t} + \nabla \cdot (\mathbf{v}\zeta_a) = F_\zeta - \frac{\zeta}{\tau_m}, \tag{1}$$

$$\frac{\partial D}{\partial t} - \mathbf{k} \cdot \nabla \times (\mathbf{v}\zeta_a) + \nabla^2\left(\frac{\mathbf{v} \cdot \mathbf{v}}{2} + \phi\right) = F_D - \nabla^2\phi_T - \frac{D}{\tau_m}, \tag{2}$$

$$\frac{\partial \phi}{\partial t} + \nabla \cdot (\mathbf{v}\phi) = F_\phi - \frac{(\phi - \phi_{\text{eq}})}{\tau_\phi}, \tag{3}$$

where $\mathbf{v}$ is the horizontal wind vector (u, v), ζ_a is absolute vorticity given by $2\Omega \sin\theta + \zeta$, Ω is the rotation rate of Earth, ∇ is the horizontal differential operator, and τ_m (τ_ϕ) is the momentum (geopotential) damping time scale. There is an additional "topographic" geopotential $\phi_T = gH_o \cos^2\theta$ or a divergence source term in Eq. (2) which is used to generate a background mean flow that conserves zonal-mean zonal angular momentum and whose strength is controlled by the parameter H_o. Here, F_ζ, F_D, and F_ϕ are generic forcing terms where the geopotential forcing F_ϕ is analogous to thermal forcing in a stably stratified fluid. As conveyed by the last term in Eq. (3), the geopotential is relaxed to a fixed value $\phi_{\text{eq}} = gh_{\text{eq}}$, where h_{eq} is the global fluid depth and g is the acceleration due to gravity. The default parameter settings are as follows unless otherwise stated: $F_D = 0$, $\tau_m = 20$ days, $\tau_\phi = 10$ days, $g = 9.8$ m s^{-2}, $\Omega = 7.29 \times 10^{-5}$ s^{-1}, and $h_{\text{eq}} = 500$ m. The terms F_ϕ and F_ζ are nonzero in the thermal and vorticity forcing experiments, respectively [see section 2a(2) for more details]. We also repeat our experiments for $h_{\text{eq}} = 200$ m to test the sensitivity of our results. The choice of h_{eq} in our experiments is justified by previous works which have shown that the MJO variance in the upper troposphere projects most strongly onto vertical mode numbers 4–10, which correspond to equivalent depths in the range of a few hundred meters. (Fulton and Schubert 1985; Žagar and Franzke 2015; Castanheira and Marques 2021; Žagar et al. 2022).

The question of how the background flow structure affects the model's steady-state response to an imposed MJO-like forcing can be addressed in at least two different ways. The first (termed "method 1") is to run the model through separate "spinup" and "forcing" stages. During the spinup stage, a stable subtropical jet is first generated by raising the zonally symmetric topography, i.e., H_o is increased from $0 \rightarrow H_{\max}$. By day 50, the model reaches an equilibrium and $H_{\max}$ determines the maximum jet speed, U_{jet}. During the subsequent forcing stage, the MJO-like forcing is switched on and the model is run further to a steady-state equilibrium, which is typically reached in 200 days. While this technique has become standard in the literature (Kraucunas and Hartmann 2007; Bao and Hartmann 2014; Monteiro et al. 2014), it can be time consuming when considering a large number of different U_{jet} profiles.

A more efficient way of probing the effects of changes in U_{jet} (termed "method 2") is to effectively combine the spinup and forcing stages. Specifically, the model is initialized with a resting basic state ($H_o = 0$) and subjected to a steady external forcing. Then over 600 days, U_{jet} is gradually increased by slowly raising the zonally symmetric topography, i.e., H_o is gradually increased from 0 to 3500 m allowing U_{jet} to span from 0 to 78 m s^{-1}, while being in quasi-steady state ($\partial U_{\text{jet}}/\partial t \rightarrow 0$). The choice of 600 days is made to ensure that the contribution of jet acceleration to the momentum budget is negligibly small. In this way, the effects of altering U_{jet} can be assessed by simply treating each stage of the integration as a separate realization of the model's steady-state response to the forcing.

In this paper, we mainly rely on method 2 to examine how the model responds to an imposed MJO-like forcing under a wide range of U_{jet} values. We ensure that a quasi-steady state is maintained throughout this process by checking that at every time step the tendency term in the momentum budget is very small relative to the remaining terms (not shown). We also performed a few runs using method 1, to ensure results are similar to those obtained using method 2 (details in appendix B).

1) DESCRIPTION OF THE BACKGROUND STATE

The specified background state is hemispherically symmetric with zero-mean winds at the equator, as an idealization of Earth's upper-tropospheric zonal-mean circulation. Figures 2a–c plot the model's steady-state zonal-mean horizontal winds $(\overline{U}, \overline{V})$ and geopotential $(\overline{\phi})$ for a range of different values of H_o. The zonal jet profile, meridional circulation and mean geopotential in all cases satisfy the following steady-state relation: $f\overline{U} + \overline{U}^2 \tan\theta/R + (1/R)\overline{V}\partial_\theta\overline{V} \approx (1/R)\partial_\theta(\overline{\phi} + \overline{\phi}_T)$, where R is the radius of Earth and θ is latitude. This relation follows from Eq. (8) in Kraucunas and Hartmann (2007) and can also be derived from Eq. (2) above. Note that the "topographic" geopotential (ϕ_T) is not present in the continuity equation [Eq. (3)] but only appears in the momentum equations [see Eq. (2)], which is required to establish a nonresting background state in the model. Conceptually, one can think of ϕ_T as representing the climatological background geopotential field in Earth's upper troposphere, due to the mean equator-to-pole temperature gradient.

In our model, as $\overline{\phi}_T$ is increased via H_o, the model's subtropical jet becomes stronger (Fig. 2a), which leads to stronger mean poleward flow (Fig. 2b) representing upper branch of the Hadley cell, along with a corresponding reduction of mean geopotential height in the tropics and buildup in the extratropics (Fig. 2c). These changes also lead to a reduction of the zonal-mean absolute vorticity gradient in the subtropics (Fig. 2d), which has an important bearing on the forcing of

[1] Original code is downloaded from https://nschaeff.bitbucket.io/shtns/shallow_water_8py-example.html and modified for the experiments.

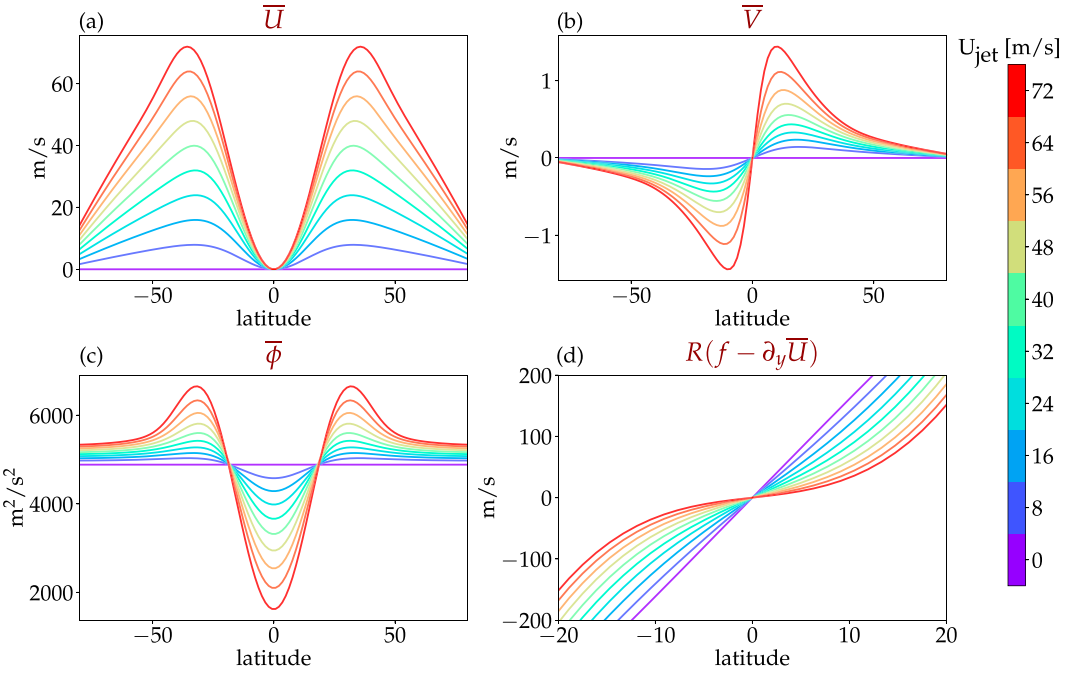

FIG. 2. Latitudinal profiles of the modeled background state (obtained using method 2; see text for details) in terms of the zonal-mean (a) zonal wind, (b) meridional wind, (c) geopotential, and (d) absolute vorticity in the tropics, color-coded for different values of U_{jet}. For convenience, absolute vorticity is scaled by the radius of Earth (R).

Rossby waves by divergent winds in the tropics (Sardeshmukh and Hoskins 1988).

2) EXTERNAL FORCING

The observed diabatic structure of the MJO typically consists of a dipole heating-and-cooling pattern that moves slowly eastward at a phase speed, $c_f \sim 5$ m s^{-1} (Jiang et al. 2020). Thus, the MJO can be considered as a near-stationary heat source when compared to free-tropospheric gravity waves, whose phase speed typically lies in the range of $c \sim 44$–70 m s^{-1} (corresponding to $h_{\text{eq}} \sim 200$–500 m). To mimic these observations, we perform a series of thermal forcing calculations, where the forcing is prescribed as a stationary dipole pattern of the form:

$$F_\phi = \frac{gQ_o}{\tau_\phi} e^{-[(\theta-\theta_o)^2/L_y^2]} F_\lambda, \tag{4}$$

where

$$F_\lambda = \begin{cases} \sin[k(\lambda-\lambda_o)] & \text{for } |(\lambda-\lambda_o)| \le 2\pi/k \\ 0 & \text{for } |(\lambda-\lambda_o)| > 2\pi/k \end{cases},$$

with the remaining forcing terms (F_ζ, F_D) set to 0. Here, Q_o is amplitude, L_y sets the meridional scale of the forcing, and k is zonal wavenumber. The default parameters are $Q_o = 10$ m, $\tau_\phi = 10$ days, $L_y = 10°$, and $k = 2$. The heating location is stationary and is centered at $\theta_o = 0°$ and $\lambda_o = 180°$. Importantly, the forcing amplitude ($Q_0 = 10$ m) is much smaller than the zonal-mean geopotential height, which ranges between 200 and 500 m in the tropics, with the precise value depending inversely on the strength of the jet (Fig. 2c). The small value of Q_o ensures that the model calculations remain approximately linear, with the nonlinear eddy terms ($\overline{\zeta' v'}$, $\overline{\zeta' \zeta'}$, etc.) being negligibly small.

As discussed later in section 3, results of the above thermal forcing experiments point to the model's tropical divergence response as being strongly affected by Rossby waves excited in the subtropics. To isolate the impact of such Rossby waves, we perform an additional vorticity forcing experiment, where the forcing F_ζ takes the form of a vorticity dipole (cyclonic-and-anticyclonic) pattern in the extratropics of both hemispheres, with the remaining forcing terms (F_ϕ, F_D) set to 0. The vorticity forcing is prescribed as

$$F_\zeta = \frac{\mathbf{k}\cdot(\nabla\times\mathbf{v}_\psi)}{\tau_m}[e^{-(\theta-40°)^2} + e^{-(\theta+40°)^2}], \tag{5}$$

where F_ζ peaks at around 40°N/S with zero value at the equator, $\tau_m = 20$ days, $\mathbf{v}_\psi$ denotes the steady-state rotational winds obtained from Helmholtz decomposition of the output from one of the stationary thermal forcing runs, namely, that with $U_{\text{jet}} = 40$ m s^{-1}, $h_{\text{eq}} = 500$ m, and the rest of the parameters having their default values. The vorticity forcing experiment is designed to isolate the effects of the Rossby gyres thermally excited by the MJO, as opposed to the effects of Rossby wave breaking/absorption excited by extratropical processes on synoptic time scales. For both the thermal and vorticity forcing experiments, we use the same set of background-mean states.

b. Analytical approach

1) MODAL DECOMPOSITION

The MJO's horizontal circulation can be viewed as a superposition of the Matsuno–Gill steady-state Kelvin and Rossby mode circulations (Gill 1980; Chao 1987; Wang and Rui 1990; Maloney and Hartmann 1998). To cast the model output in these terms, we perform a meridional mode decomposition using parabolic cylinder functions (PCFs). The approach is similar to that of Yang et al. (2003), which enables separation of the model's steady-state response into contributions by 1) the Kelvin mode, 2) the lowest-order Rossby mode, and 3) the remaining (symmetric) higher-order Matsuno modes, where the term "higher/lower order," refers to the meridional index number n of the associated PCFs. Stated mathematically,

$$\begin{pmatrix} u^* \\ v^* \\ \phi^* \end{pmatrix} = \underbrace{\begin{pmatrix} u_K \\ v_K \\ \phi_K \end{pmatrix}}_{\text{Kelvin}} + \underbrace{\begin{pmatrix} u_R \\ v_R \\ \phi_R \end{pmatrix}}_{\text{Rossby}} + \underbrace{\begin{pmatrix} u_{\text{HO}} \\ v_{\text{HO}} \\ \phi_{\text{HO}} \end{pmatrix}}_{\text{Higher-order}}, \tag{6}$$

where asterisks denote zonal eddies (i.e., $u^* = u - \overline{U}$). The Kelvin (K), Rossby (R), and higher-order (HO) Matsuno modes are calculated using Eqs. (A5)–(A7), respectively (see appendix A). In our steady-state model response, the $n = 1$ mode is dominated by the Rossby component, as shown in Fig. A2. Additionally, there are no forced asymmetric modes (like the mixed Rossby–gravity mode), since the background-mean state and forcing are both symmetric about the equator.

In a resting basic state ($U_{\text{jet}} = 0$), these modes correspond to the orthogonal eigenvectors of the linearized shallow water system on an equatorial beta plane (Matsuno 1966; Gill 1980). In a nonresting basic state ($U_{\text{jet}} > 0$), the modes still form a complete orthonormal basis, but are only approximations of the actual eigenvectors, whose structures are somewhat modified due to the effects of the background flow (Zhang and Webster 1992). From Eq. (6), the horizontal eddy divergence can be decomposed as

$$\nabla \cdot \mathbf{v}^* = \nabla \cdot \mathbf{v}_K + \nabla \cdot \mathbf{v}_R + \nabla \cdot \mathbf{v}_{\text{HO}}, \tag{7}$$

where $\mathbf{v}^*$ denotes horizontal eddy wind vector (u^*, v^*), $\mathbf{v}_K$ denotes (u_K, v_K), $\mathbf{v}_R$ denotes (u_R, v_R), and $\mathbf{v}_{\text{HO}}$ denotes (u_{HO}, v_{HO}). Equation (7) is evaluated in sections 3a(2) and 3b. In the case of spherical geometry, the Kelvin mode may have weak meridional wind signals, v_K, depending on the choice of equivalent depth and zonal wavenumber (Kasahara 1980; Žagar et al. 2015). However, for simplicity we assume $v_K \approx 0$.

2) VORTICITY BUDGET DECOMPOSITION

In addition to the above modal decomposition, we diagnose the model eddy divergence from the steady-state vorticity relation [Eq. (1)], which can be expressed as $\nabla \cdot (\mathbf{v}\zeta_a)^* \approx F_\zeta^*$, assuming damping is weak. Linearizing the above relation about a zonally symmetric background state ($\overline{U}$, $\overline{V}$) and neglecting the nonlinear terms, the steady-state eddy divergence can then be decomposed as

$$\nabla \cdot \mathbf{v}^* \approx \underbrace{\frac{-v^*\beta_{\text{eff}}}{\overline{\zeta}_a}}_{\text{Sverdrup effect}} + \underbrace{\frac{-\partial_y(\overline{V}\zeta^*)}{\overline{\zeta}_a}}_{\text{Hadley cell effect}} + \underbrace{\frac{-\overline{U}\partial_x\zeta^*}{\overline{\zeta}_a}}_{\text{Jet advection}} + \underbrace{\frac{F_\zeta^*}{\overline{\zeta}_a}}_{\text{Vorticity forcing}}, \tag{8}$$

where ζ^* is relative eddy vorticity and $\beta_{\text{eff}} = \beta - \partial_{yy}\overline{U}$. The horizontal derivatives in Cartesian coordinates are $\partial_x = \partial_y(\cdot)/R$ and $\partial_y = \partial_\theta[(\cdot)\cos\theta]/(R\cos\theta)$. Each term on the right-hand side (rhs) of Eq. (8) is given a name that alludes to the dynamical process embodied by the numerator of that term. For example, the first term is referred to as the "Sverdrup effect" (Gill 1980; Monteiro et al. 2014), since it represents the portion of divergence that can be attributed to eddy meridional advection of the background absolute vorticity. The second term is referred to as the "Hadley cell effect," since it represents the portion that can be attributed to meridional deposition of the eddy vorticity flux by the mean meridional winds. Likewise, the third term is referred to as the "jet advection," since it represents the zonal advection of eddy vorticity by the zonal-mean zonal winds. And finally, the fourth term is the "vorticity forcing," which represents the contribution to divergence from external sources, which in the real world may involve nonlinear eddy–eddy interaction. In the thermal forcing experiments, F_ζ^* is set to zero.

Note that in Eq. (8) the denominator, $\overline{\zeta}_a$ goes to zero near the equator (Fig. 2d), but not all the numerators tend to zero at the same rate leading to an issue of division by zero, especially in the Hadley cell term for very high jet speeds. For presentation purposes and to avoid infinities, we latitudinally smooth each of the rhs terms in Eq. (8) using the Savitzky–Golay filter of polynomial order 3 and window length 25. Equation (8) is evaluated in sections 3a(3) and 3a(4).

3. Results

a. Steady-state response to thermal forcing and variable jet speed

We first focus on the impact of the subtropical jet on the MJO's thermally forced circulation in the upper troposphere with the fluid depth h_{eq} set at 500 m and U_{jet} ranging from 0 to 78 m s^{-1}. Setting $h_{\text{eq}} = 500$ m ensures that the model runs stably for a large range of jet values and the tropical fluid depth stays close to the real world (200–500 m), with the precise value depending inversely on the strength of the jet (Fig. 2c).

1) SUBTROPICAL RESPONSE

Figure 3 shows the steady-state eddy geopotential and wind anomalies excited by the stationary MJO-like thermal forcing for different subtropical jet speeds. The steady-state circulation obtained from method 2 is comparable to method 1 except for some minor differences which do not affect our overall results (see appendix B and Fig. B1 for a detailed comparison between methods 1 and 2). In the familiar case where $U_{\text{jet}} = 0$ (Fig. 3a), the positive part of the forcing induces a

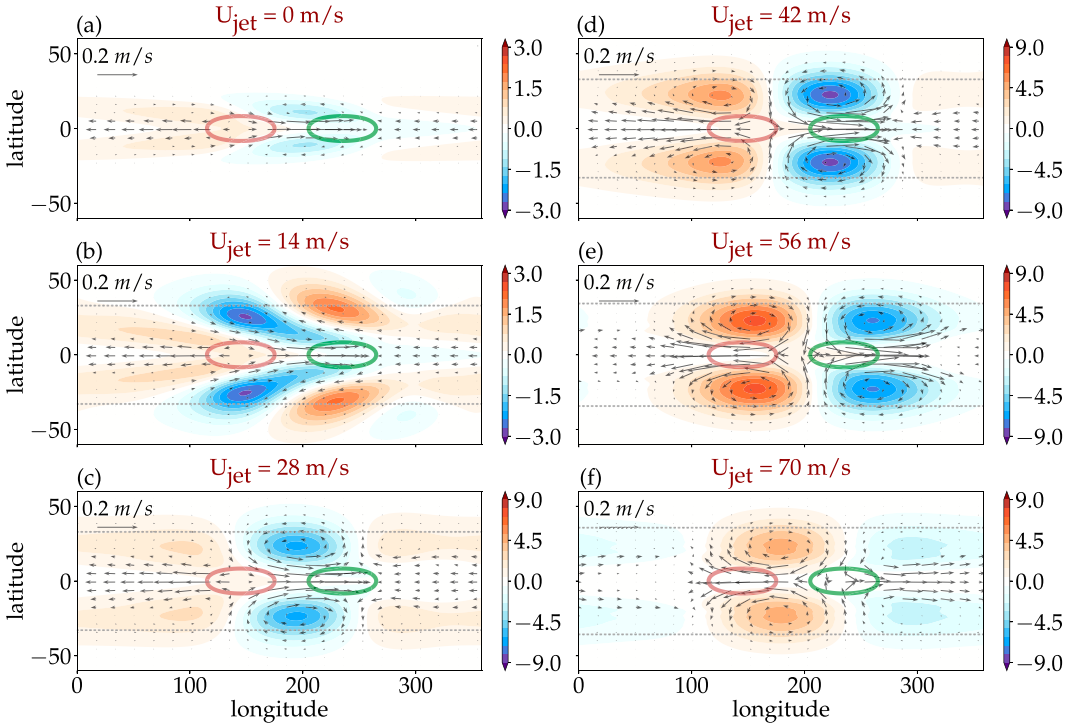

FIG. 3. Steady-state response to fixed MJO-like thermal forcing in terms of the eddy geopotential ϕ^* (colors; $m^2\ s^{-2}$) and eddy wind vectors $\mathbf{v}^*$ ($m\ s^{-1}$) for background jet speeds U_{jet} of (a)–(f) 0, 14, 28, 42, 56, and 70 $m\ s^{-1}$, respectively. Positive and negative thermal forcing regions are shown in brown and green contours, respectively, which represent 1/4 of the maximum forcing. The dotted lines show the location of the jet maxima. Note the two different color bars used for (a) and (b) versus (c)–(f).

classic Gill-like pattern, consisting of a stationary Kelvin wave to the east and equatorial Rossby wave to the west of the mass source or heating region (Gill 1980). This same Rossby–Kelvin pattern is also excited by the mass sink or cooling region, but with opposite sign. As the jet speed increases, the equatorial Rossby wave response amplifies and shifts poleward, while the overall stationary wave pattern becomes meridionally tilted (shown for U_{jet} = 14 m s^{-1} in Fig. 3b). The tilted structure of the Rossby response (Fig. 3b) gives the impression of a teleconnection pattern due to weak waveguiding effect of the subtropical jet (Ambrizzi et al. 1995; Branstator and Teng 2017). In contrast, for the stronger jets, i.e., $U_{jet} \geq$ 28 m s^{-1}, the equatorial Rossby waves transform into prominent subtropical gyres that are meridionally trapped due to stronger waveguiding effect and are advected eastward with respect to the forcing (Figs. 3c–f). See online supplementary Fig. S1 for more details.

This systematic shift from an equatorial waveguide to a wider subtropical stationary wave pattern due to imposed changes in background jet strength was first reported by Monteiro et al. (2014), using a similar shallow water model setup. In addition to those authors' findings, we observe an interesting threshold behavior that has not been previously documented. Qualitatively, the overall strength of the subtropical gyres, as measured by their maximum magnitude of geopotential anomalies, is seen to increase monotonically for $U_{jet} \approx$ 0–42 m s^{-1} while it decreases for $U_{jet} \approx$ 42–70 m s^{-1}.

An important difference between the model used here versus that of Monteiro et al. (2014) is in terms of the formulation of the geopotential tendency equation. Specifically, while those authors assumed a linearized geopotential flux, i.e., $\phi_{eq}(\nabla \cdot \mathbf{v})$ [see Eq. (3) in their supplementary material], here we include the full geopotential flux term, i.e., $\nabla \cdot (\phi \mathbf{v})$ [Eq. (3)]. As shown later, this difference has important implications for the divergent part of the eddy response in the tropics, whose dependence on jet speed is documented below.

2) TROPICAL RESPONSE

Figure 4 shows the divergent part of the steady-state circulation for different values of U_{jet}, where the divergent flow ($\mathbf{v}_\chi$) is determined using the Helmholtz decomposition. The picture is broadly consistent with expectations, where net outflow from the heating region is balanced by net inflow to the cooling region. As the jet speed increases, the off-equatorial divergence and convergence associated with the subtropical cyclonic and anticyclonic vortices become more prominent on the poleward flanks of the forcing region (see Figs. 4d–f). In the case of very strong jet speeds ($U_{jet} \geq$ 42 m s^{-1}), the meridional component of the divergent winds become increasingly dominant over the zonal component, implying a transition in the dominant type of waves elicited by the forcing. Interestingly, the increase in U_{jet} also leads to an increase in the magnitude of the eddy divergence at the forcing region. To leading

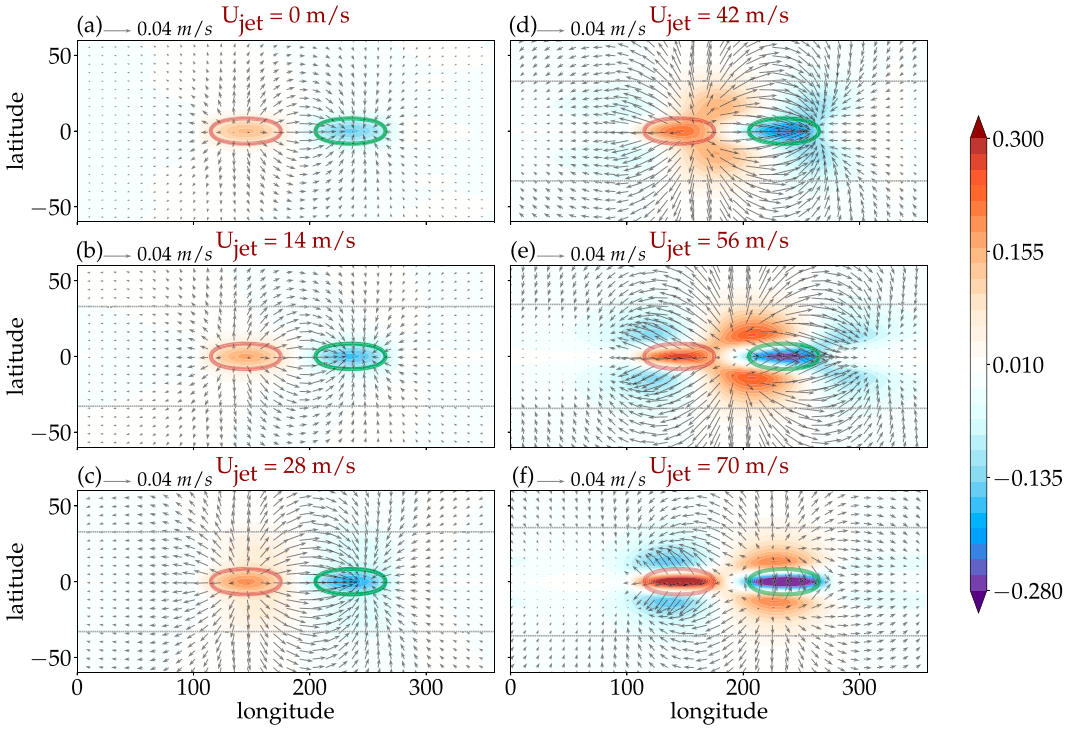

FIG. 4. Steady-state response to fixed MJO-like thermal forcing in terms of eddy divergence $R\nabla\cdot\mathbf{v}^*$ (colors; m s^{-1}) and divergent eddy wind vectors $\mathbf{v}^*_\chi$ (m s^{-1}) for background jet speeds U_{jet} set as (a)–(f) 0, 14, 28, 42, 56 and 70 m s^{-1}, respectively. Positive and negative thermal forcing regions are shown in brown and green contours, respectively, which represent 1/4 of the maximum forcing. The dotted lines show the location of the jet maxima. Divergence is rescaled by the radius of Earth (R) for convenience.

order, the relation between eddy divergence and the jet speed near the forcing region can be understood by considering the following steady-state approximation of the linearized geopotential equation, Eq. (3),

$$\langle\overline{\phi}\rangle D^* \approx \langle F^*_\phi\rangle, \tag{9}$$

where angle brackets denote latitudinal averaging between 10°S and 10°N, overline denotes zonal mean and $D^* = \langle\nabla\cdot\mathbf{v}^*\rangle$. The remaining linear terms, namely, $\overline{U}\partial_x\phi^*$, $\partial_y(\phi^*\overline{V})$, and $v^*\partial_y\overline{\phi}$ are dropped from Eq. (9), since they are found to be of negligible value when averaged between 10°S and 10°N. By gradient wind balance, we know that $\langle\overline{\phi}\rangle$ decreases with increasing jet speed (Fig. 2c), meaning eddy divergence (convergence) must increase in the heating (cooling) region to balance the fixed thermal forcing.

It is worth mentioning here that Eq. (9) is a statement of the weak-temperature gradient (WTG) approximation for a shallow water system [see Eq. (4) in Sobel et al. 2001]. Therefore, we define the quantity, $\widetilde{D^*} \equiv F^*_\phi/\langle\overline{\phi}\rangle$, as the WTG divergence and use it as a baseline for interpreting changes in the actual divergence D^*. In a vertically stratified system, the equivalent geopotential, $\langle\overline{\phi}\rangle$ can be interpreted as the ratio of tropical static stability (Γ) to the vertical scale of the convective heating (L_z), i.e., $\langle\overline{\phi}\rangle = \Gamma/L_z$ [see Eq. (14) in Kiladis et al. 2009]. The implication is that the WTG divergence associated with MJO is linked to all three factors, namely, upper-level adiabatic heating/cooling, tropical static stability, and the vertical heating profile, all of which could be modified by the subtropical jet.

Globally, since the imposed net mass source is zero, the area-averaged eddy divergence must also be zero. However, in the vicinity of the forcing region the eddy divergence shows a clear jet speed dependence, despite the thermal forcing being constant. To capture the local amplification of the eddy divergence anomalies in the tropics, Fig. 5a shows the root-mean-square of D^* averaged within the latitude band 10°S–10°N (D^*_{RMS}; cyan curve in Fig. 5a). To leading order, the increase of D^*_{RMS} with increasing jet speed broadly matches with the expectation from WTG approximation ($\widetilde{D^*}_{\text{RMS}}$; orange curve in Fig. 5a). However, the agreement is by no means perfect. The deviation between the actual divergence and WTG approximation ($\delta_{\text{RMS}} = D^*_{\text{RMS}} - \widetilde{D^*}_{\text{RMS}}$) grows with increasing jet speed and reaches a maximum, before eventually decreasing and becoming negative (purple curve in Fig. 5a). This deviation is interesting and confirms that the jet-speed dependence of the model's tropical divergence involves more than just the effect of changing $\langle\overline{\phi}\rangle$ as a consequence of gradient wind balance. The changes in δ_{RMS} primarily arise from the latitudinal variation in mean geopotential. In other words, if the WTG relation [Eq. (9)] is modified to include $v^*\partial_y\overline{\phi}$ term then the orange curve exactly matches with the cyan curve in Fig. 5a (not shown). This implies that the latitudinal variation in static stability and its

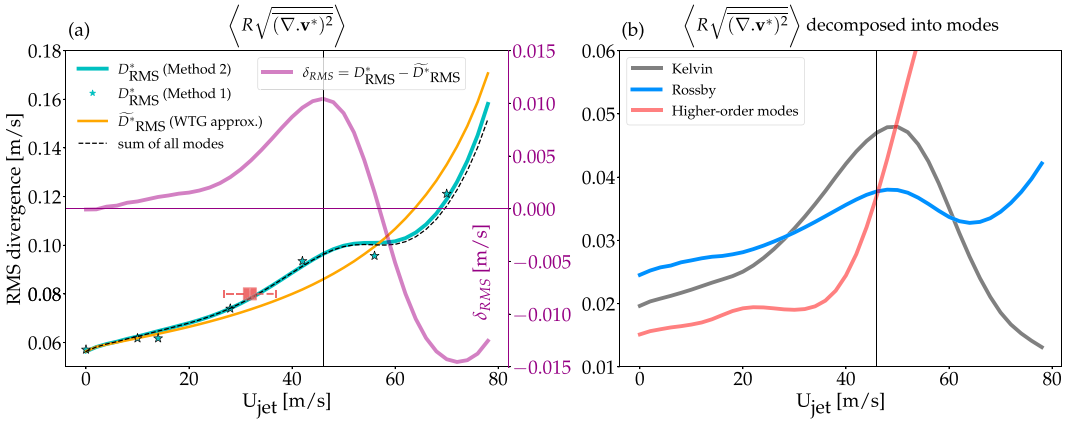

FIG. 5. Jet-speed dependence of (a) RMS eddy divergence in the tropics obtained from the model run (D^*_{RMS}; left y axis), the WTG approximation ($\widetilde{D}^*_{\mathrm{RMS}}$; left y axis), and the difference between the two (δ_{RMS}; right y axis) and (b) D^*_{RMS} decomposed into Kelvin, Rossby, and higher-order Matsuno modes [using Eq. (7)]. In (a), the red boxplot marks the seasonal mean and interannual variability of subtropical jet speed during wintertime (1979–2019) from ERA5, the stars and the solid cyan curve denote results from running steady-state experiments using method 1 and 2, respectively, and the black dashed curve is the linear sum of all the modes from Eq. (7). The black vertical line indicates an estimated critical jet speed U_c (see text for details). The RMS divergence is calculated for the latitude band 10°S–10°N and then rescaled by the radius of Earth, R.

interaction with the subtropical eddies could also impact the MJO-induced tropical divergence.

To emphasize the threshold behavior of the divergent part of the response, we define a critical jet speed, $U_c = 46$ m s^{-1} at which δ_{RMS} reaches its peak value (black vertical line in Fig. 5a). The precise value of U_c is found to depend on the specified gravity wave speed ($c = \sqrt{gh_{\mathrm{eq}}}$) and the phase speed of the thermal forcing (c_f) (Fig. C1 in appendix C). It is plausible that a critical jet speed (U_c) also exists in the real world whose value is close to 46 m s^{-1}. Earth's strongest subtropical jet (~32 ± 5 m s^{-1}) occurs during boreal winter over the IPAC region (20°–55°N, 30°E–180°), implying the MJO's divergence signals may be most strongly affected by the subtropical jet during this season versus others.

To break down the response of D^*_{RMS} further, Fig. 5b shows how changes in U_{jet} affect the RMS eddy divergence for the Kelvin mode, lowest-order Rossby mode, and higher-order Matsuno modes [see Eqs. (6) and (7) for modal decomposition]. As U_{jet} is increased, the Kelvin-mode amplitude (gray curve in Fig. 5b) increases gradually before reaching its peak value at roughly the critical jet speed U_c and then decreases sharply thereafter. This behavior is different from that of the Rossby mode, whose amplitude (blue curve in Fig. 5b) exhibits only modest deviations about an overall gradual increase across the entire span of U_{jet} values. The amplitude of the higher-order Matsuno modes (red curve in Fig. 5b) remains relatively small for jet speeds below ~35 m s^{-1}, but increases sharply thereafter and eventually becomes dominant for $U_{\mathrm{jet}} > U_c$.

To summarize, the jet-speed dependence of the divergent part of the response to an imposed MJO-like thermal forcing exhibits two distinct regimes: (i) a "weak-jet" regime ($U_{\mathrm{jet}} < U_c$) where the deviation between actual divergence and WTG divergence near the forcing region (δ_{RMS}) grows with the increase in jet speed mainly due to stronger amplification of Kelvin divergence and (ii) a "strong-jet" regime ($U_{\mathrm{jet}} > U_c$) where the deviation (δ_{RMS}) is reduced and becomes negative with increasing jet speed mainly due to a reduction in Kelvin divergence, despite the increased contribution by the higher-order Matsuno modes. In both jet regimes, the WTG divergence anomaly projects onto the steady-state forced Kelvin mode, as opposed to free Kelvin waves whose phase speed can be considered as infinite under the WTG approximation (Bretherton and Sobel 2003; Ahmed et al. 2021).

3) WEAK-JET REGIME

To identify the key dynamical processes regulating the jet-speed dependence of the model's divergence response, we decompose the eddy divergence from the steady-state vorticity budget to reflect contributions from the Sverdrup effect, the Hadley cell effect, and jet advection [Eq. (8)]. Figure 6 shows the divergence decomposition for the weak-jet cases using Eq. (8). As expected from the steady-state mass balance, eddy divergence at the forcing region is positive over the heat source and negative over the heat sink (Figs. 6a-i–d-i). In the absence of a jet, the local eddy divergence at the forcing region is primarily balanced by the Sverdrup effect (Fig. 6a-i) and has no contribution from the Hadley cell effect or jet advection. As the jet speed strengthens, the Sverdrup effect also strengthens and amplifies the local eddy divergence (Figs. 6a-ii–d-ii), particularly in the eastern flank of the forcing region due to zonally advected subtropical gyres (Fig. 3). With the increase in jet speed, the Hadley cell effect increases but has relatively weaker magnitude (Figs. 6a-iii–d-iii) and the jet advection counteracts the increase in local eddy divergence although its effect is only strong at latitudes poleward of the forcing region (Figs. 6a-iv–d-iv).

The important role of the Sverdrup effect in the weak-jet regime suggests that any change in divergence at the forcing region is dynamically controlled by off-equatorial interactions

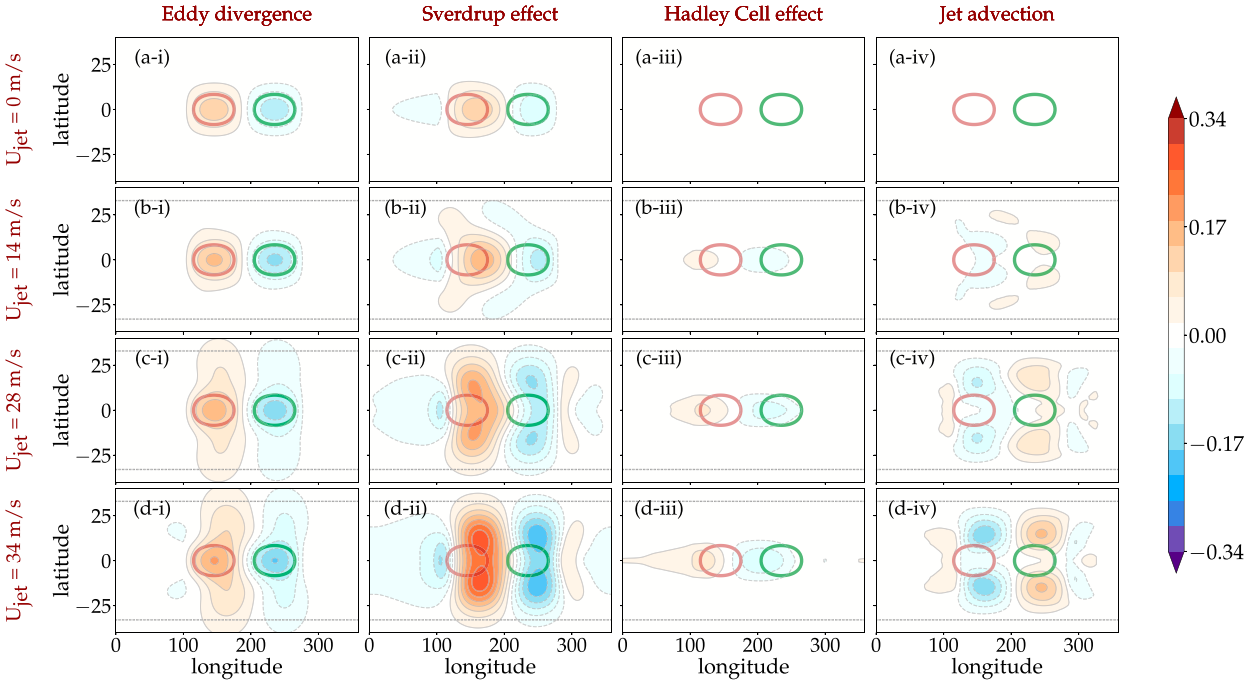

FIG. 6. Divergence budget for the weak-jet regime ($U_{\text{jet}} < U_c$) as defined in Eq. (8) where (i) total eddy divergence is decomposed into contribution from (ii) Sverdrup effect, (iii) Hadley cell effect, and (iv) jet advection where U_{jet} is set as (a)–(d) 0, 14, 28, and 34 m s^{-1}, respectively. Divergence is rescaled by the radius of Earth (R) and is shown in units of m s^{-1} (colors). Positive and negative thermal forcing regions are shown in brown and green contours where contours represent 1/4 of the maximum forcing. The dotted line shows the location of the jet maxima.

between the eddy subtropical meridional wind (v^*) and the zonal-wind meridional shear ($\partial_y \overline{U}$), which is expressed as

$$\Delta(\nabla \cdot \mathbf{v}^*) \approx \Delta\left(\frac{-v^* \beta_{\text{eff}}}{f - \partial_y \overline{U}}\right), \tag{10}$$

where Δ denotes change between two equilibrium states with different jet speeds. Note that close to equator, we can approximate zonal-mean zonal wind as a parabolic function of y, i.e., $\overline{U} \approx (1/2)U_0'' y^2$, where U_0'' is a constant (see Fig. 2a). Following this, $\beta_{\text{eff}} \approx \beta - U_0''$, $f - \partial_y \overline{U} \approx (\beta y - U_0'' y)$. So the ratio $v^* \beta_{\text{eff}}/(f - \partial_y \overline{U})$ scales as (v^*/y) close to the equator. Thus, Eq. (10) implies that the increase/decrease of eddy divergence must be determined by the amplitude of meridional eddy winds ($|v^*|$) which predominantly comes from a strengthening Rossby wave source in the presence of stronger subtropical jet. To test this, we further decompose Eq. (10) into individual tropical modes as

$$\Delta D_K + \Delta D_R + \Delta D_{\text{HO}} \approx \underbrace{\Delta\left(\frac{-v_K \beta_{\text{eff}}}{f - \partial_y \overline{U}}\right)}_{\text{Sv}_K} + \underbrace{\Delta\left(\frac{-v_R \beta_{\text{eff}}}{f - \partial_y \overline{U}}\right)}_{\text{Sv}_R} + \underbrace{\Delta\left(\frac{-v_{\text{HO}} \beta_{\text{eff}}}{f - \partial_y \overline{U}}\right)}_{\text{Sv}_{\text{HO}}}, \tag{11}$$

where $D = \nabla \cdot \mathbf{v}^*$, Sv denotes Sverdrup effect, and the subscripts K, R, and HO denote Kelvin, Rossby, and higher-order Matsuno modes, respectively. The modal decomposition of the other terms (e.g., Hadley cell effect, jet advection) are omitted from Eq. (11), since they are not dominant for the weak-jet regime (Fig. 6).

Figure 7 captures the change in divergence/convergence and the change in Sverdrup effect for $U_{\text{jet}} = 34$ m s^{-1} (Fig. 6d) minus the $U_{\text{jet}} = 0$ m s^{-1} (Fig. 6a) decomposed into individual tropical modes as in Eq. (11). We find that near the heat source (heat sink) the increase in divergence (convergence) is primarily due to amplification of the Kelvin mode (Fig. 7a-i), while anomalies for the Rossby and higher-order Matsuno modes are negligible near the forcing (Figs. 7a-ii,a-iii). At the same time, the Sverdrup change is dominated by the Rossby mode and has an amplifying effect on eddy divergence/convergence at the forcing region (notice the same signs in Figs. 7b-ii,a-i). There is little to no Sverdrup effect from the Kelvin and higher-order Matsuno modes (Figs. 7b-iii,b-i).

The weak-jet regime may be the most relevant for Earth's upper troposphere since the zonal-mean subtropical jet is rarely found to be any stronger than ~30–40 m s^{-1}. This relevance points to a possible jet–MJO feedback mechanism which can be summarized as follows. As long as the jet speed is below a critical value ($U_{\text{jet}} < U_c$), a stronger jet leads to a stronger MJO-forced subtropical Rossby mode, which by the Sverdrup effect, amplifies the equatorial Kelvin mode and hence, MJO convective heating.

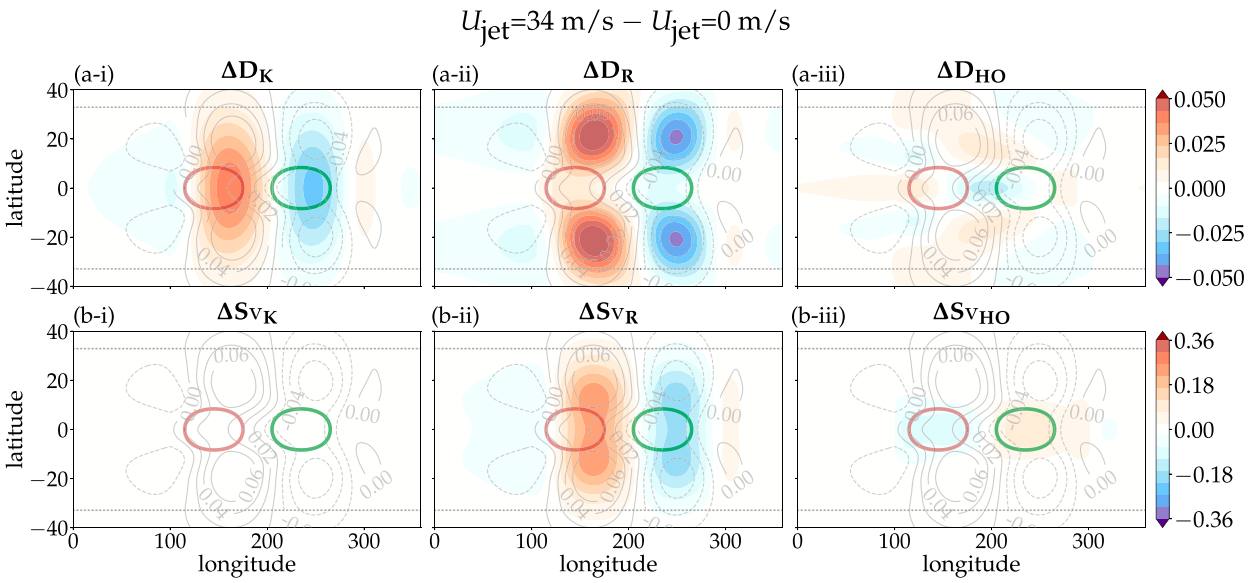

FIG. 7. Change in (a) eddy divergence and (b) Sverdrup effect between subtropical jet-state (U_{jet} = 34 m s^{-1}) and resting basic-state (U_{jet} = 0 m s^{-1}) experiments. Each row is decomposed into contributions from (i) Kelvin, (ii) Rossby, and (iii) higher-order Matsuno modes as defined in Eq. (11). Gray solid (dashed) contours denote increase (decrease) in total divergence and is given by the sum of (a-i), (a-ii), and (a-iii). Divergence is rescaled by the radius of Earth (R) and is shown in units of m s^{-1} (colors). Positive and negative thermal forcing regions are shown in brown and green contours where contours represent 1/4 of the maximum forcing.

4) STRONG-JET REGIME

For jet speeds greater than the critical value ($U_{jet} > U_c$), we see a regime shift in the role of dynamical processes that affect the local eddy divergence at the forcing region. Figure 8 shows the divergence decomposition for the strong-jet cases using Eq. (8). Again, eddy divergence at the forcing region is positive over the heat source and negative over the heat sink (Figs. 8a-i–d-i). In contrast to the weak-jet cases, the Hadley cell effect plays the most important role in amplifying the local eddy divergence (Figs. 8a-iii–d-iii) while the Sverdrup effect

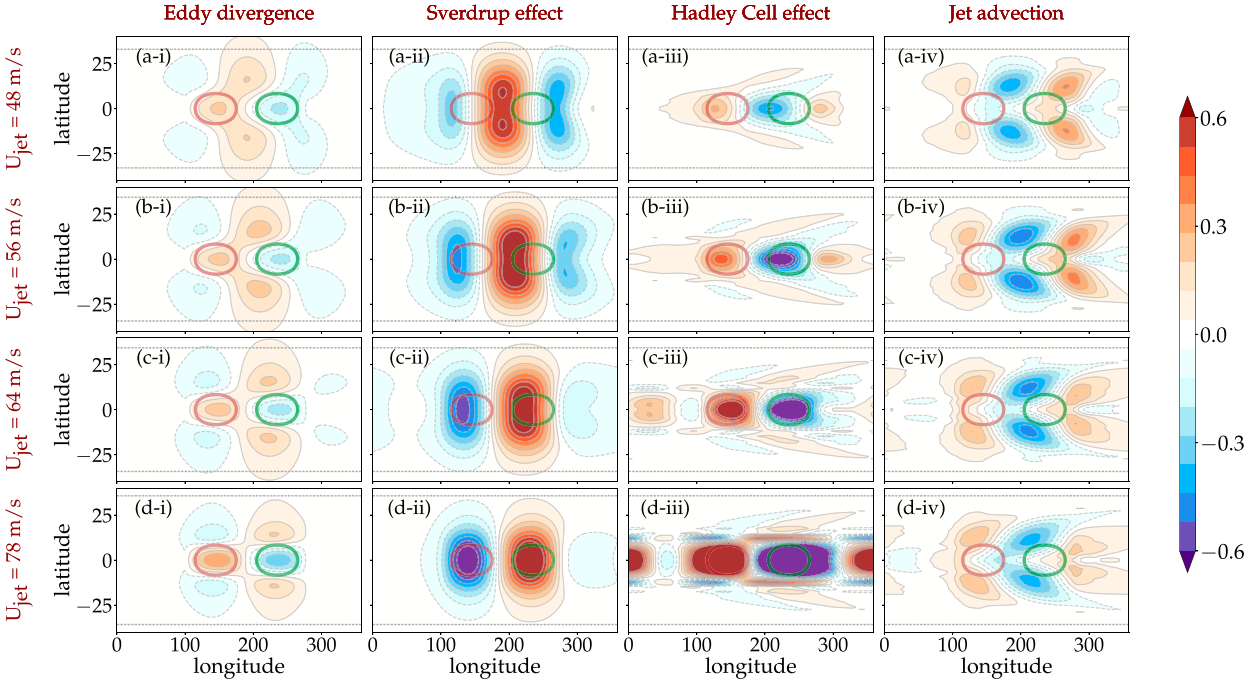

FIG. 8. As in Fig. 6, but for the strong-jet regime ($U_{jet} > U_c$).

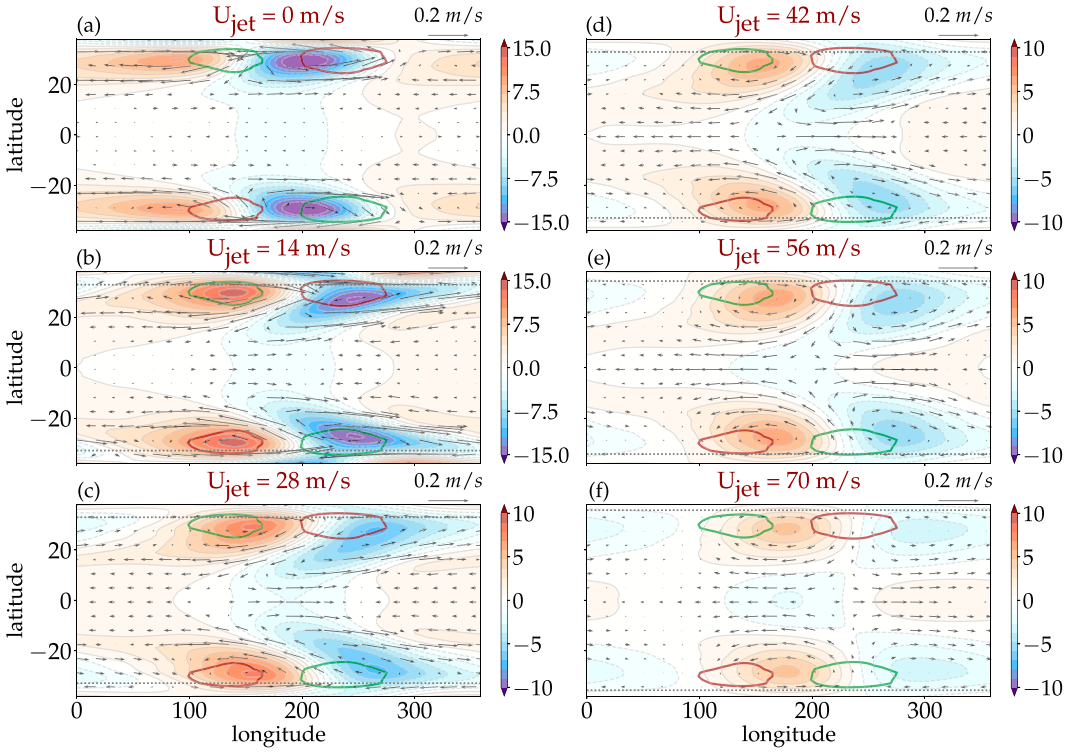

FIG. 9. As in Fig. 3, but for the vorticity forcing experiments where brown and green contours show 1/4 of the maximum positive and negative forcing, respectively. The dotted lines show the location of the jet maxima. Note the two different color bars used for (a) and (b) versus (c)–(f).

attenuates it (Figs. 8a-ii–d-ii). For all cases, jet advection has an almost negligible role on the local divergence; rather, its effect is only strong outside of the forcing region (Figs. 6a-iv–d-iv).

In the strong-jet regime, while the subtropical Rossby mode is quite pronounced (Figs. 3e,f and A2e,f), the tropical divergence associated with the MJO is dominated by higher-order Matsuno modes rather than the Kelvin mode (Fig. 5b). The strong-jet regime may be relevant for climate change scenarios or other planetary systems where the subtropical jet and the Hadley cell could be stronger than what is presently observed on Earth. For even stronger jet speeds ($U_{\text{jet}} > 80$ m s^{-1}) the model becomes nonlinear and unstable, which may indicate another regime transition toward equatorial superrotation (Showman and Polvani 2011; Potter et al. 2014; Zurita-Gotor and Held 2018).

To stay relevant to Earth's atmosphere, here we focus on the weak-jet regime ($U_{\text{jet}} < U_c$), where a stronger jet amplifies both the subtropical Rossby mode and the equatorial Kelvin mode. Further decomposition of the eddy divergence from the vorticity budget reveals that the Kelvin divergence and Rossby winds are linked to one another via the Sverdrup effect. This result leads naturally to the question of whether a remotely forced Rossby mode can amplify the Kelvin mode in the absence of tropical heat source?

b. *Steady-state response to vorticity forcing and variable jet speed*

To answer the above, we performed a vorticity forcing experiment, involving a sequence of quasi-steady states produced using method 2 for a range of jet speeds, under no thermal forcing and a stationary vorticity forcing in the subtropics resembling the quadrupole Rossby gyres associated with the MJO. The vorticity forcing is specified by imposing the subtropical cyclonic and anticyclonic vortices derived from one of the steady states in the thermal forcing experiment, namely, that with $U_{\text{jet}} = 40$ m s^{-1} [see section 2a(2) and Eq. (5) for details].

Figure 9 shows the steady-state eddy geopotential and wind anomalies excited in response to the same vorticity forcing under different subtropical jet speeds. In the case of no jet, the vorticity forcing induces a strong local response in the subtropics and negligible response in the tropics ($\theta < 15$°N/S) (Fig. 9a). When a jet is present, the same vorticity forcing induces a remote tropical response that gets stronger with increasing jet speed, as well as a local subtropical response that weakens proportionately, indicating a transfer of energy from the subtropics to the tropics (Figs. 9b–f). For $U_{\text{jet}} = 56$ and 70 m s^{-1}, the tropical response acquires a well-defined Kelvin structure indicated by the same phase of zonal winds (u^*) and geopotential (ϕ^*) eddies equatorward of 15°N/S (Figs. 9e,f). This suggests that even in the absence of equatorial thermal forcing, subtropical Rossby gyres are able to induce a shear-mediated Kelvin response. When the vorticity forcing is shifted poleward of the jet maxima, we find very weak to no tropical response for the range of jet speeds considered (not shown).

Figure 10 shows the strength of steady-state tropical divergence anomalies (measured by D^*_{RMS}) for different values of jet speed in the vorticity forcing experiment (cf. with Fig. 5).

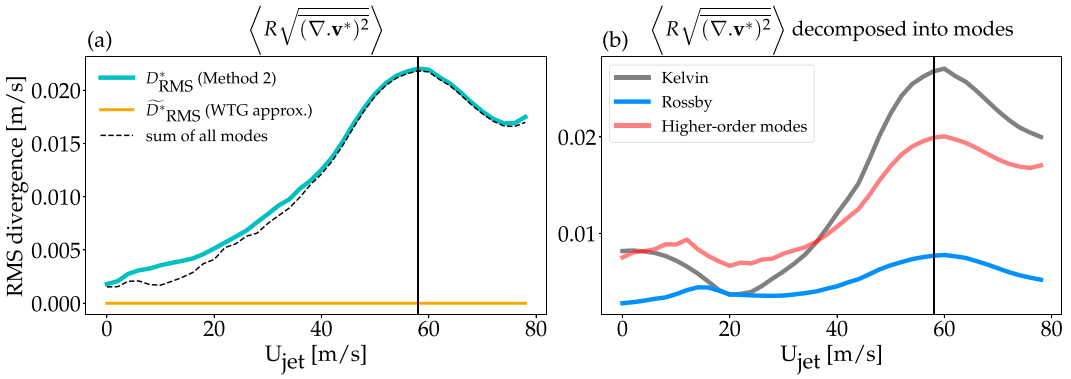

FIG. 10. As in Fig. 5, but for the vorticity forcing experiments.

When forced with a "gyre-like" vorticity source in the subtropics, D^*_{RMS} increases with increasing jet speed up to $U_{\mathrm{jet}} = 58$ m s^{-1} (see cyan curve in Fig. 10a). This behavior is similar to that found in the thermal forcing experiment (cf. with Fig. 5), except that the vorticity-induced divergence anomalies in the tropics cannot be explained by the WTG approximation ($\widetilde{D^*}_{\mathrm{RMS}}$) since $\langle F^*_\phi\rangle/\langle\overline{\phi}\rangle = 0$ in the absence of thermal forcing at the equator (see orange dashed curve in Fig. 10a). Furthermore, by decomposing the eddy divergence into individual Matsuno modes (using the PCF projection method as outlined in section 2b), we find that Kelvin mode dominates the overall increase in D^*_{RMS}, especially for jet speeds higher than 38 m s^{-1} (gray curve in Fig. 10b). The contribution by higher-order Matsuno modes is comparatively weaker for stronger jet values (red curve in Fig. 10b), while the Rossby contribution is the weakest (blue curve in Fig. 10b). Interestingly, we also find a critical threshold at a slightly higher jet speed of 58 m s^{-1} where D^*_{RMS} (dominated by the Kelvin mode) decreases with increasing jet speed.

To identify the key dynamical processes behind the jet-speed dependence of the model's divergent response, we focus on the Sverdrup effect [Eq. (10)] of the vorticity forcing experiment. In the weak-jet regime (i.e., $U_{\mathrm{jet}} < 58$ m s^{-1}), other divergent sources [from Eq. (8)], namely, Hadley cell effect, jet advection, and vorticity forcing are also present but they do not dominate tropical divergence (not shown). Figure 11 shows the change in divergence/convergence and the change in Sverdrup effect for $U_{\mathrm{jet}} = 56$ m s^{-1} (Fig. 9e) minus the $U_{\mathrm{jet}} = 0$ m s^{-1} (Fig. 9a) decomposed into individual tropical modes as in Eq. (11). At the equatorial region, we find that an increase in divergence (convergence) is primarily due to an amplification of the Kelvin mode (Fig. 11a-i) while the divergence/convergence from Rossby and higher-order Matsuno modes are weaker near the equator (Figs. 11a-ii,a-iii). At the same time, the Sverdrup change is dominated by the Rossby mode and has

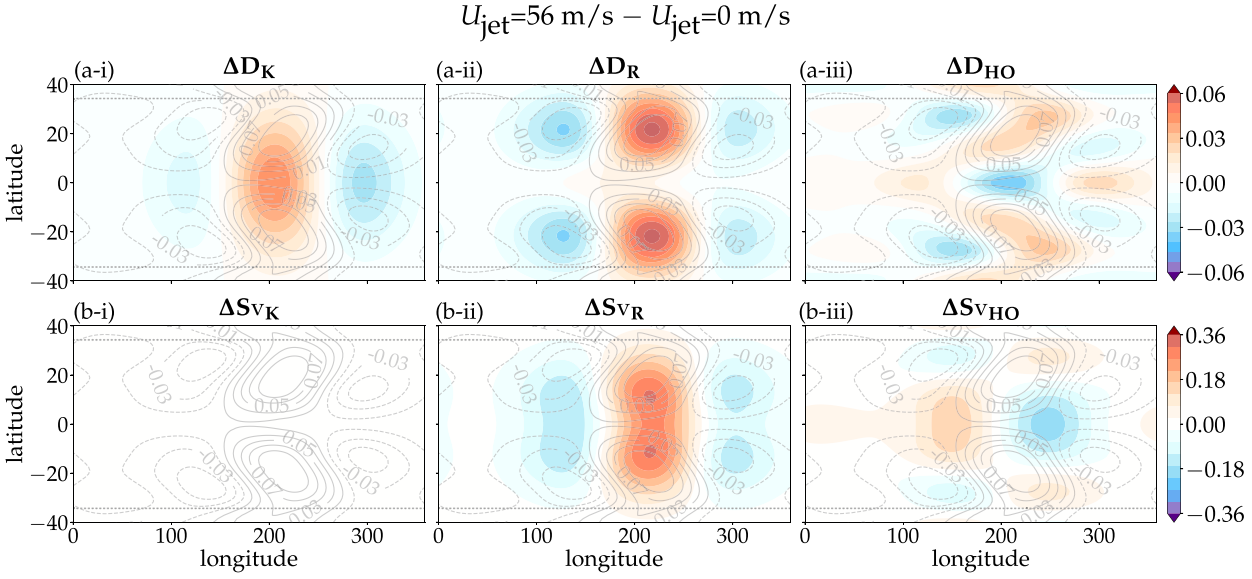

FIG. 11. As in Fig. 7, but for vorticity forcing experiments showing change in (a) eddy divergence and (b) Sverdrup effect between subtropical jet state ($U_{\mathrm{jet}} = 56$ m s^{-1}) and resting state ($U_{\mathrm{jet}} = 0$ m s^{-1}).

an amplifying effect on eddy divergence/convergence at the equator (see the same signs in Figs. 11b-ii and a-i). There is little to no Sverdrup effect from the Kelvin and higher-order Matsuno modes (Figs. 7b-iii,b-i).

In summary, our results confirm that in the absence of equatorial thermal forcing, subtropical Rossby gyres are able to induce a shear-mediated Kelvin response, which increases in strength as the jet speed increases up to a critical value. It should be kept in mind that these findings do not imply the Kelvin-mode component of the MJO is produced solely by subtropical Rossby gyres. Rather, the point is that the Kelvin- and Rossby-mode components of the MJO are closely linked to one another via the Sverdrup effect. If the subtropical Rossby gyres are strengthened by external processes [for, e.g., via low-frequency variability in the extratropics (Lin et al. 2007; Lin and Brunet 2011) or via changes in the subtropical jet due to Arctic warming (Barnes and Screen 2015)], then their effect will be felt by the Kelvin-mode circulation component of the MJO, potentially leading to strengthening of MJO convection, in accordance with the idealized MJO simulations of TK21. In other words, the subtropical Rossby gyres are coupled to the Kelvin mode not just by convective heating but also by the zonal-mean meridional wind shear. It is the latter feature of the basic state that enables the Rossby gyres to act as a "Kelvin wave source" for the tropics, in much the same way that tropical heating can act as "Rossby wave source" for the extratropics (Sardeshmukh and Hoskins 1988).

Interestingly, the shear-mediated coupling is the strongest when U_{jet} is approximately equal to the dry gravity wave speed in the tropics (Figs. 5b and 10b) indicating a phase speed resonance between the Doppler-shifted subtropical Rossby gyres and the equatorial Kelvin mode. This behavior is consistent with some other studies that have emphasized the idea of resonant coupling between midlatitudes and the tropics (Majda and Biello 2003; Wang and Xie 1996; Hoskins and Yang 2000; Cheng et al. 2022).

4. Discussion and conclusions

a. *Potential implications on the vertical structure and amplitude of the MJO*

Based on our modeling result, we hypothesize two feedback mechanisms by which the subtropics can affect the MJO's horizontal circulation. The first is governed by WTG balance and implies that if the tropical static stability and/or vertical heating profile respond to changes in the subtropical jet strength, then the MJO's thermally forced divergence anomalies ($\widetilde{D}^*$) should increase with increasing jet speed regardless of jet regime. It is not clear yet how effectively this mechanism operates in the real world, since static stability in the tropics is believed to be strongly constrained by moist thermodynamic processes (Stone and Carlson 1979; Betts 1982; Xu and Emanuel 1989). However, some recent studies have shown that such thermodynamic constraints may not be as strict, enabling large-scale circulations to modify free-tropospheric lapse rates (Bao et al. 2022). The cause-and-effect relationship under WTG balance constraints is therefore not clear, and warrants further investigation.

The second feedback mechanism involves deviations from strict WTG balance in the form of shear-mediated coupling between Kelvin and Rossby waves, via the "Sverdrup effect." The Sverdrup effect is the most important mechanism that couples subtropics to a deep tropical Kelvin response and is most strongly felt when the jet speed is between 40 and 60 m s^{-1}. Our results imply that there is a critical jet speed at which the Kelvin-mode divergence of the MJO is maximized due to the impact of the mean flow on subtropical eddies. We speculate that our current climate may be operating in the weak-jet regime where the mean subtropical jet is weaker than the critical value, but approaches the critical limit during boreal winter. Long-term climate variability (longer than the intraseasonal time scales) may alter the relative jet speed with respect to its critical value and affect the MJO's convective amplitude via Rossby–Kelvin feedback. While beyond the scope of this paper, we plan to test this conjecture using general circulation model (GCM) experiments in a future work.

In reality, both feedback mechanisms may be operating simultaneously and could provide a conceptual framework for understanding 1) the MJO's response to quasi-biennial oscillation (QBO) phases via changes in subtropical jet speed (Garfinkel and Hartmann 2011a,b; Gray et al. 2018; Martin et al. 2021), 2) the MJO's response to different climate change scenarios (Carlson and Caballero 2016), and 3) the cause of MJO biases in global climate models (Ahn et al. 2020). However, it is important to remember that the conclusions drawn here are based on a highly simplified model with no moisture or cloud radiative processes where heating patterns associated with the MJO is imposed. For instance, we do not know how much of the convective outflow generated by the upper-level feedback couples to the low-level MJO convergence/divergence. Depending on the strength of the vertical coupling, it may have different effects on vertical motion, cloud distribution and moisture feedback, which may in turn affect the phase speed and the amplitude of the MJO.

b. *Linear versus nonlinear MJO dynamics*

It should also be noted that the forced circulations studied here were derived by running a nonlinear shallow water model in a stable linear regime. This approach is physically meaningful, because MJO composites from ERA5 dataset reveal that the zonal momentum budget of the MJO during boreal winter is dominated by the linear advection terms (not shown), in accordance with several other observational studies (e.g., Lin et al. 2005; Sakaeda and Roundy 2014, 2015).

However, our approach conflicts with several dry MJO theories that describe the MJO either as a nonlinear phenomenon driven by extratropical forcing (Wedi and Smolarkiewicz 2010; Yano and Tribbia 2017; Rostami and Zeitlin 2020) or a heavily damped Kelvin wave with no role for Rossby waves (Kim and Zhang 2021). TK21 also highlighted the role of nonlinear momentum fluxes on the MJO, but they did not evaluate the impact of the linear terms. The effects of nonlinearities might be important for the transient (onset or decay stage) or

in moist feedback processes of the MJO. However, the problem of MJO maintenance can be simply explained on the basis of linear dynamics. The linear Rossby–Kelvin feedback mechanism in the lower troposphere may also aid in the eastward propagation of the MJO as noted by Hayashi and Itoh (2017) and might also explain why the MJO tends to be stronger in the Indo-Pacific region, where the subtropical jet is the strongest and closest to the equator during wintertime. The Rossby–Kelvin coupling also plays an important role in meridional moisture advection by the MJO as recently noted by Berrington et al. (2022).

Note that our conclusions about linear Rossby–Kelvin interaction is derived from simple modal decomposition that makes the β-plane approximation on a sphere [see section 2b(1)]. These results could be improved in future by using more sophisticated technique such as the spherical normal mode decomposition as shown by some recent MJO studies (Kosovelj et al. 2019; Kitsios et al. 2019; Franzke et al. 2019).

c. Concluding remarks

Previous studies on MJO dynamics have shown that moisture, cloud radiation, and boundary layer processes (Zhang et al. 2020, and references therein) play a crucial role in MJO's initiation and propagation, which we consider as given. Here we focus on the impact of the wintertime subtropical jet in the Indo-Pacific region which sits just north of the MJO dipole and creates substantially strong upper-level horizontal shear for equatorial convective systems. The mean-flow interaction between MJO convection and the jet gives rise to planetary-scale Rossby gyres in the subtropical upper troposphere, which forms an integral part of the MJO's circulation (Sardeshmukh and Hoskins 1988; Adames and Wallace 2014; Monteiro et al. 2014). The question of whether these forced Rossby gyres and jet structure have any subsequent feedback onto the tropics is much less understood. Recently TK21 found considerable weakening of MJO-like signals in idealized SP-WRF calculations when the zonal-mean zonal jet was weakened by 25%, while other parameters like static stability and surface temperature were kept constant.

To understand this result, we used a dry spherical shallow water model to examine how the divergent part of its response to an MJO-like thermal forcing is affected by the presence and strength of an imposed subtropical jet. Results showed a positive correlation between equatorial divergence/convergence and subtropical jet speed, but with two different regimes of behavior (weak jet versus strong jet). In the weak-jet regime, the MJO-induced divergence is amplified due to the "Sverdrup effect," while in the strong-jet regime, the divergence amplifies due to the "Hadley cell effect."

To leading order, the divergence induced by the forcing was seen to be well explained by WTG balance ($\widetilde{D^*}$), in accordance with other studies (Sobel et al. 2001; Wolding et al. 2017). In addition, we found a second-order divergence effect (δ_{RMS}) which peaks at a critical jet speed, U_c and primarily comes from the shear-mediated coupling between subtropical Rossby gyres and the tropical Kelvin mode. This coupling interpretation was further supported by an additional vorticity experiment, which showed how the imposition of subtropical gyre-like forcing induces a Kelvin-mode response near the equator that is strongly dependent on the jet speed. Despite the use of a nonlinear model, all the processes were found to be predominantly linear, in accordance with the imposed small-amplitude forcing and the absence of any intrinsic mean-flow instability.

Regardless of the simplicity of the model setup, our results point to the potentially important feedback mechanisms by which the presence of a subtropical jet can affect the MJO's structure and amplitude. Future developments of MJO theory should therefore consider the role of the upper-tropospheric subtropical background flow on the precise nature of the phenomenon.

Acknowledgments. We thank Maria Gehne, Nedjeljka Žagar, Joseph Biello, and one anonymous reviewer for their comments and suggestions which substantially improved the clarity of the paper. P. Barpanda is grateful to Joy Monteiro for his help in setting up the shallow water model and thanks Brandon Wolding and Yuan-Ming Cheng for helpful discussions during the project. This research was supported in part by NOAA Cooperative Agreement NA22OAR4320151 and National Science Foundation (NSF) through Award AGS-1839741. P. Barpanda also acknowledges support from NOAA and CIRES for the postdoc opportunity.

Data availability statement. The ERA5 data can be accessed through the ECMWF website (https://www.ecmwf.int/en/forecasts/datasets/reanalysis-datasets/era5). The scripts for running shallow water model experiments can be accessed from https://github.com/Pragallva/MJO-waves-mean-flow.

APPENDIX A

Meridional Mode Decomposition

The dry equatorial waves, i.e., Kelvin, Rossby, mixed Rossby–gravity (MRG), and inertia–gravity (IG) modes, were originally derived by Matsuno (1966) as orthonormal eigen modes of an unforced linear shallow water system on an equatorial β plane with a resting basic state. Later Gill (1980) extended this problem and showed that the steady-state solution to a forced shallow water system is a linear superposition of Rossby, Kelvin, and MRG modes (IG modes decay to zero in a damped steady state). The Matsuno–Gill modes (hereafter Matsuno modes) have a characteristic meridional structure, given by the PCF of degree m, which is expressed as

$$D_m\left(\frac{\theta}{\theta_T}\right) = 2^{-m/2}\exp\left[-\frac{1}{2}\left(\frac{\theta}{\theta_T}\right)^2\right]H_m\left(\frac{\theta}{\theta_T}\right), \tag{A1}$$

where various parameters in Eq. (A1) are defined as follows: $H_m(\theta/\theta_T)$ is the physicist's Hermite polynomial of degree $m \geq 0$, θ is latitude in radians, $\theta_T = (1/R)\sqrt{c/\beta}$ is the equatorial trapping scale in radians, and $\beta = 2\Omega/R$, where Ω and R are the angular velocity and radius of Earth, respectively. Replacing β with $\beta - \partial_{yy}\overline{U}$ did not change the modal decomposition results, so we used the same trapping scale, θ_T for all

U_{jet} experiments. Instead of PCFs [Eq. (A1)] one could also use spherical normal modes or Hough functions for modal decomposition. Note this may lead to somewhat different trapping scale (θ_T) of the wave modes (Žagar et al. 2015).

Our shallow water system is neither on a β plane nor does it have a resting basic state (spherical model with a background horizontal shear). However, the final steady-state solutions can be approximated as linear superposition of Matsuno modes up to meridional truncation number N. This is the same as Galerkin method of discretization and has been successfully used in reanalysis dataset for identifying equatorial waves (Yang et al. 2003; Gehne and Kleeman 2012; Knippertz et al. 2022; Haertel 2022). We take the same approach for decomposing our steady-state shallow water model response into Matsuno modes as described below.

We define new variables, q, r, v from the model output where $q = u^* + \phi^*/c$, $r = u^* - \phi^*/c$, and $v = v^*$. The denominator $c = \sqrt{gh_{\text{eq}}}$ is the average gravity wave speed of the shallow water model where $h_{\text{eq}} = 500$ m The variables, q, r, and v can be expressed as the weighted sum of the orthogonal PCF modes, i.e.,

$$q(\lambda, \theta) = q_0(\lambda)D_0(\theta/\theta_T) + q_1(\lambda)D_1(\theta/\theta_T) + \sum_{n\geq 1}^{N} q_{n+1}(\lambda)D_{n+1}(\theta/\theta_T), \tag{A2}$$

$$v(\lambda, \theta) = \sum_{n\geq 1}^{N} v_n(\lambda)D_n(\theta/\theta_T), \tag{A3}$$

$$r(\lambda, \theta) = \sum_{n\geq 1}^{N} r_{n-1}(\lambda)D_{n-1}(\theta/\theta_T), \tag{A4}$$

where n is an integer and $N = 10$ is the meridional truncation number and Matsuno mode coefficients are given by (q_{n+1}, v_n, r_{n-1}). Using Matsuno's (1966) convention, $n = -1$ corresponds to the Kelvin mode whose coefficients are (q_0, 0, 0); $n = 0$ corresponds to the MRG mode whose coefficients are (q_1, 0, 0), $n = 1$ corresponds to the lowest-order Rossby mode whose coefficients are (q_2, v_1, r_0), and $n \geq 2$ correspond to other higher-order Matsuno modes whose coefficients are (q_{n+1}, v_n, r_{n-1}).

Each of the coefficients in Eqs. (A2)–(A4) is determined by projecting the nth-order PCF on to q, r, and v, respectively, and using the orthogonality relation for PCF functions. For example, $v_n(\lambda) = [1/(\sqrt{\pi}n!\theta_T)]\int_{-\pi/2}^{+\pi/2} v(\lambda, \theta)D_n(\theta/\theta_T)d\theta$ for $n \geq 0$. The same projection formula applies to other coefficients q_n and r_n.

Once all the mode coefficients (q_{n+1}, v_n, r_{n-1}) are determined, the eigenvector for each mode in terms of winds and geopotential can be expressed as follows:

- Kelvin:

$$\begin{pmatrix} u_K \\ v_K \\ \phi_K \end{pmatrix} = \frac{1}{2}\begin{pmatrix} q_0 D_0 \\ 0 \\ c(q_0 D_0) \end{pmatrix}; \tag{A5}$$

- Rossby:

$$\begin{pmatrix} u_R \\ v_R \\ \phi_R \end{pmatrix} = \frac{1}{2}\begin{pmatrix} q_2 D_2 + r_0 D_0 \\ v_1 D_1 \\ c(q_2 D_2 - r_0 D_0) \end{pmatrix}; \tag{A6}$$

- Higher order:

$$\begin{pmatrix} u_{\text{HO}} \\ v_{\text{HO}} \\ \phi_{\text{HO}} \end{pmatrix} = \frac{1}{2}\begin{pmatrix} \sum_{n>2}^{N}(q_{n+1}D_{n+1} + r_{n-1}D_{n-1}) \\ \sum_{n>2}^{N}(v_n D_n) \\ \sum_{n>2}^{N} c(q_{n+1}D_{n+1} - r_{n-1}D_{n-1}) \end{pmatrix}. \tag{A7}$$

For the same set of thermal forcing experiments documented in the main text (Fig. 3), Figs. A1–A3 show the decomposition of steady-state response into individual Kelvin, Rossby, and higher-order Matsuno modes as outlined in section 2b(1).

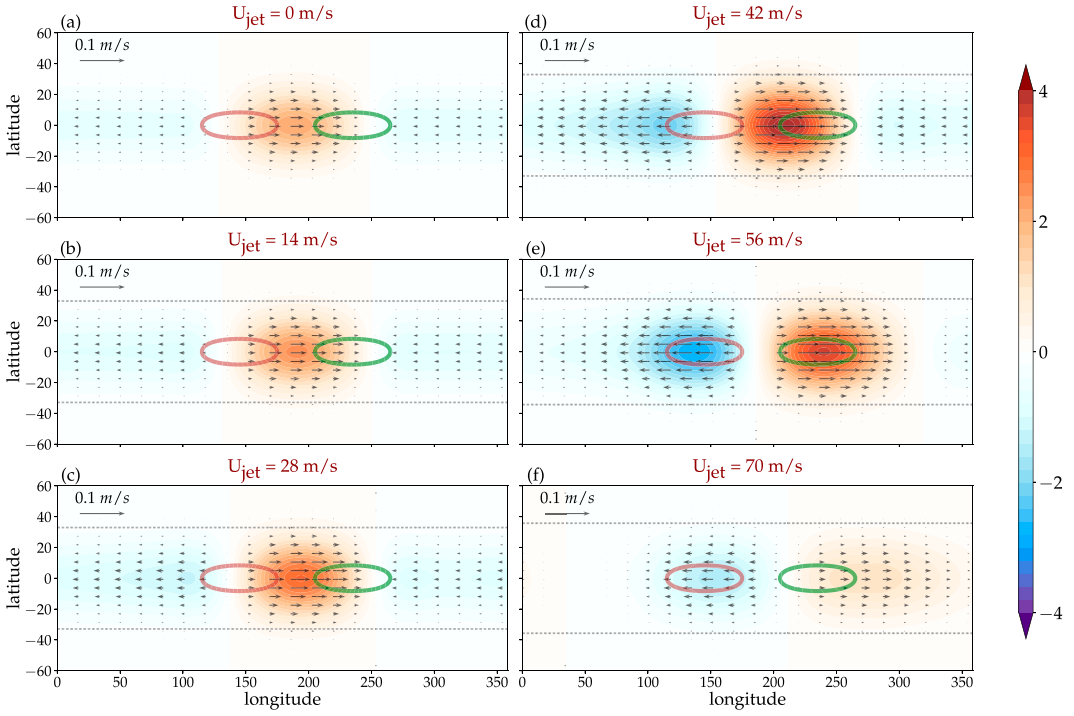

FIG. A1. As in Fig. 3, but for Kelvin-mode component of the circulation showing eddy geopotential (ϕ_K^*; colors; m^2 s^{-2}) and wind vectors ($\mathbf{v}_K^*$; m s^{-1}) as defined in Eqs. (6) and (A5).

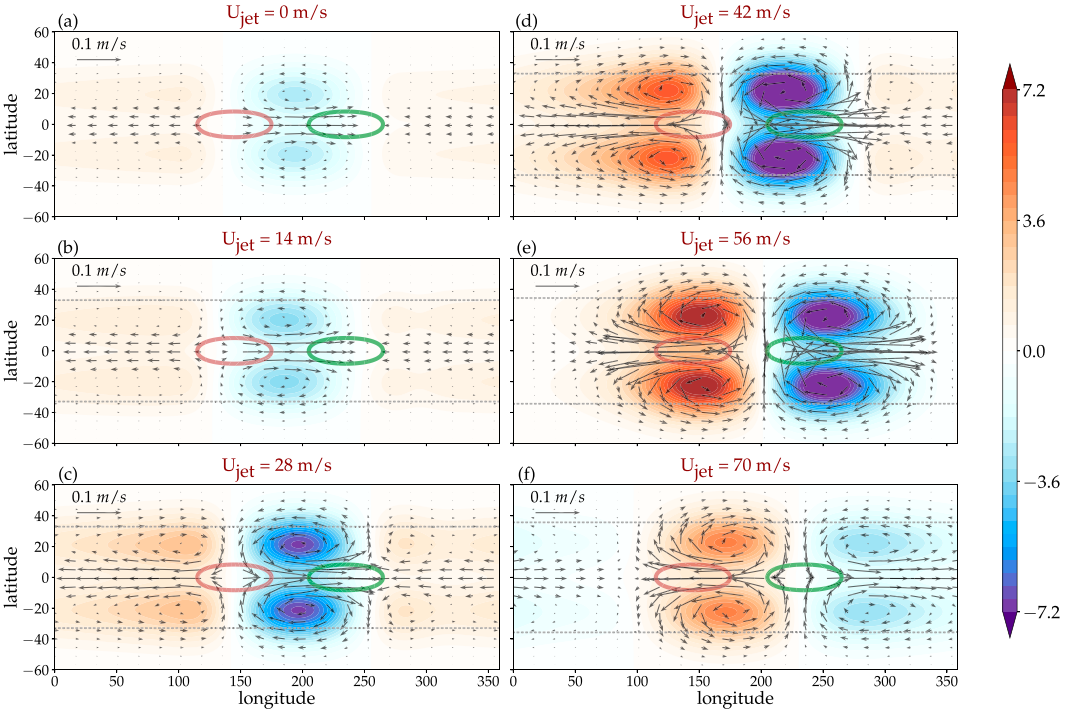

FIG. A2. As in Fig. 3, but for Rossby-mode component of the circulation showing eddy geopotential (ϕ_R^*; colors; m^2 s^{-2}) and wind vectors ($\mathbf{v}_R^*$; m s^{-1}) as defined in Eqs. (6) and (A6).

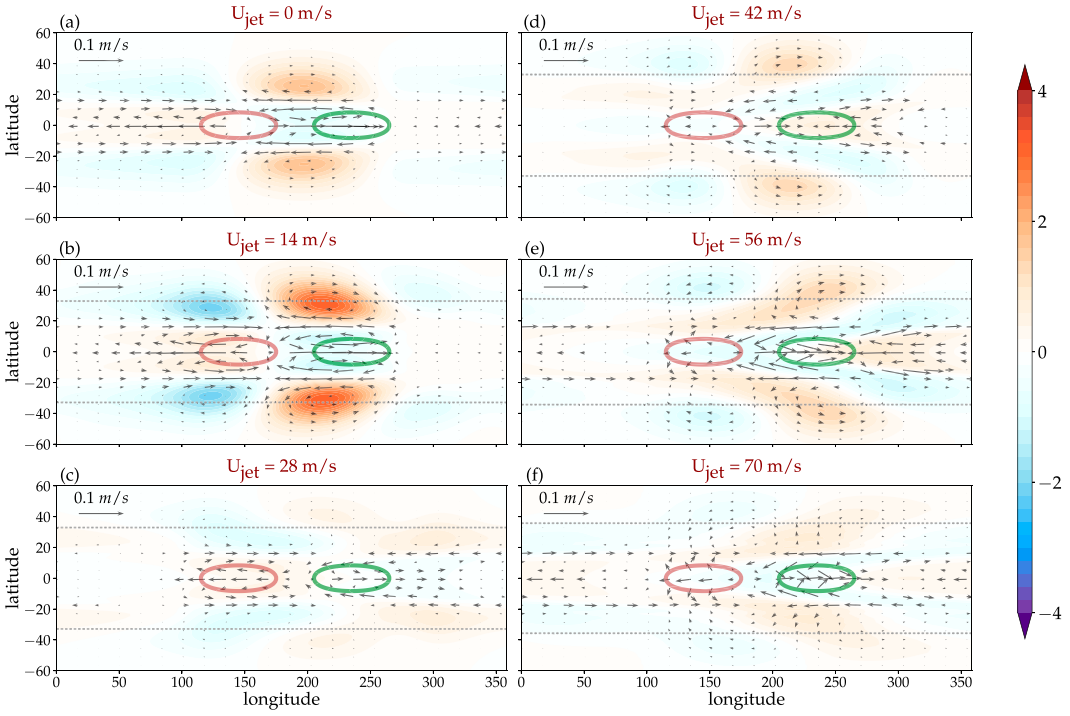

FIG. A3. As in Fig. 3, but for higher-order Matsuno modes showing eddy geopotential (ϕ^*_{HO}; colors; $m^2\ s^{-2}$) and wind vectors ($\mathbf{v}^*_{HO}$; $m\ s^{-1}$) as defined in Eqs. (6) and (A7).

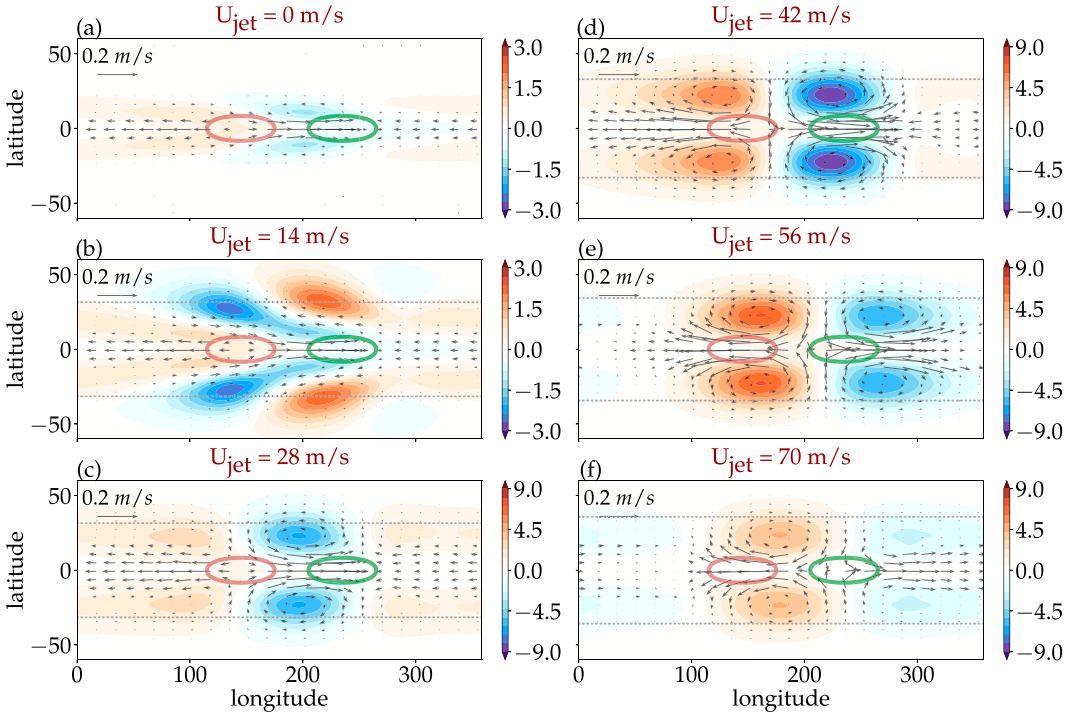

FIG. B1. Steady-state response to fixed thermal forcing and changing jet speeds. As in Fig. 3, but calculated using method 1.

APPENDIX B

Steady-State Model Response Using Method 1

Here we highlight our results from an ensemble of six steady-state shallow water model experiments, each initialized with different jet speeds (0, 14, 28, 42, 56, 70 m s^{-1}) but forced with the same MJO-like thermal forcing (see a detailed description of method 1 in section 2a). The steady-state circulation anomalies from six method 1 runs (Fig. B1) are very similar to those obtained from a single quasi-steady state run using method 2 (Fig. 3). Method 1 also captures the threshold behavior of the subtropical gyres as noted in the main text. Although there are some differences in the magnitude of the responses and the peak location of the gyres, the errors are negligible and do not affect the main conclusions of the paper as evidenced by method 1 results shown in Fig. 5a.

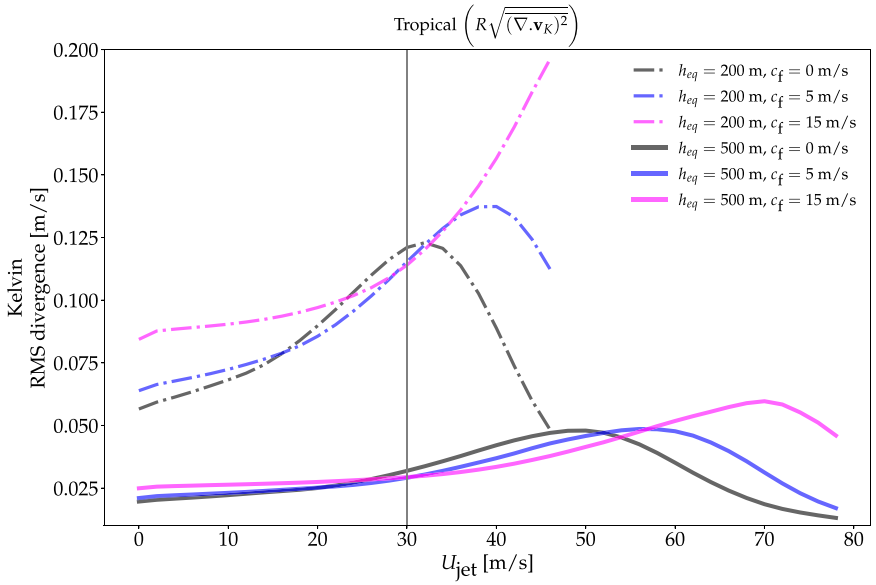

FIG. C1. RMS Kelvin divergence in the tropics in response to thermal forcing with different phase speeds (c_f), different jet speeds (U_{jet}), and different equivalent depths (h_{eq}). The RMS divergence is averaged over 10°S–10°N and is rescaled by the radius of Earth (R). The black vertical line indicates Earth's zonal-mean jet speed in the Northern Hemisphere during winter.

APPENDIX C

Sensitivity of Kelvin Divergence to Changing Equivalent Depth and Forcing Phase Speeds

Here we explore the sensitivity of our experiments to changing equivalent depths, which is a measure of effective static stability in the atmosphere and an imposed thermal forcing moving at different forcing phase speed, c_f. Figure C1 captures results from several thermal forcing experiments showing root-mean-square of Kelvin divergence (averaged between 10°S and 10°N) for a wide range of jet speeds for two equivalent depths (h_{eq} = 200 and 500 m) and 3 different forcing phase speeds (c_f = 0, 5, and 15 m s^{-1}) but with a fixed heating amplitude. Note that the critical jet speed (U_c) is not a constant; rather, it is lowered for smaller gravity wave speed ($c = \sqrt{gh_{\text{eq}}}$) and smaller forcing phase speed (c_f), i.e., U_c is small when c and c_f are small.

REFERENCES

Adames, A. F., and J. M. Wallace, 2014: Three-dimensional structure and evolution of the vertical velocity and divergence fields in the MJO. *J. Atmos. Sci.*, **71**, 4661–4681, https://doi.org/10.1175/JAS-D-14-0091.1.

Ahmed, F., J. D. Neelin, and Á. F. Adames, 2021: Quasi-equilibrium and weak temperature gradient balances in an equatorial beta-plane model. *J. Atmos. Sci.*, **78**, 209–227, https://doi.org/10.1175/JAS-D-20-0184.1.

Ahn, M.-S., and Coauthors, 2020: MJO propagation across the Maritime Continent: Are CMIP6 models better than CMIP5 models? *Geophys. Res. Lett.*, **47**, e2020GL087250, https://doi.org/10.1029/2020GL087250.

Ambrizzi, T., B. J. Hoskins, and H.-H. Hsu, 1995: Rossby wave propagation and teleconnection patterns in the austral winter. *J. Atmos. Sci.*, **52**, 3661–3672, https://doi.org/10.1175/1520-0469(1995)052<3661:RWPATP>2.0.CO;2.

Bao, J., V. Dixit, and S. C. Sherwood, 2022: Zonal temperature gradients in the tropical free troposphere. *J. Climate*, **35**, 7937–7948, https://doi.org/10.1175/JCLI-D-22-0145.1.

Bao, M., and D. L. Hartmann, 2014: The response to MJO-like forcing in a nonlinear shallow-water model. *Geophys. Res. Lett.*, **41**, 1322–1328, https://doi.org/10.1002/2013GL057683.

Barnes, E. A., and J. A. Screen, 2015: The impact of Arctic warming on the midlatitude jet-stream: Can it? Has it? Will it? *Wiley Interdiscip. Rev.: Climate Change*, **6**, 277–286, https://doi.org/10.1002/wcc.337.

Berrington, A. H., N. Sakaeda, J. Dias, and G. N. Kiladis, 2022: Relationships between the eastward propagation of the Madden–Julian oscillation and its circulation structure. *J. Geophys. Res. Atmos.*, **127**, e2021JD035806, https://doi.org/10.1029/2021JD035806.

Betts, A. K., 1982: Saturation point analysis of moist convective overturning. *J. Atmos. Sci.*, **39**, 1484–1505, https://doi.org/10.1175/1520-0469(1982)039<1484:SPAOMC>2.0.CO;2.

Branstator, G., and H. Teng, 2017: Tropospheric waveguide teleconnections and their seasonality. *J. Atmos. Sci.*, **74**, 1513–1532, https://doi.org/10.1175/JAS-D-16-0305.1.

Bretherton, C. S., and A. H. Sobel, 2003: The Gill model and the weak temperature gradient approximation. *J. Atmos. Sci.*, **60**, 451–460, https://doi.org/10.1175/1520-0469(2003)060<0451:TGMATW>2.0.CO;2.

Carlson, H., and R. Caballero, 2016: Enhanced MJO and transition to superrotation in warm climates. *J. Adv. Model. Earth Syst.*, **8**, 304–318, https://doi.org/10.1002/2015MS000615.

Castanheira, J. M., and C. A. F. Marques, 2021: The equatorial wave skeleton of the Madden–Julian oscillation. *Quart. J. Roy. Meteor. Soc.*, **147**, 3778–3788, https://doi.org/10.1002/qj.4156.

Chao, W. C., 1987: On the origin of the tropical intraseasonal oscillation. *J. Atmos. Sci.*, **44**, 1940–1949, https://doi.org/10.1175/1520-0469(1987)044<1940:OTOOTT>2.0.CO;2.

Cheng, Y.-M., S. Tulich, G. N. Kiladis, and J. Dias, 2022: Two extratropical pathways to forcing tropical convective disturbances. *J. Climate*, **35**, 6587–6609, https://doi.org/10.1175/JCLI-D-22-0171.1.

Ferranti, L., T. N. Palmer, F. Molteni, and E. Klinker, 1990: Tropical–extratropical interaction associated with the 30–60 day oscillation and its impact on medium and extended range prediction. *J. Atmos. Sci.*, **47**, 2177–2199, https://doi.org/10.1175/1520-0469(1990)047<2177:TEIAWT>2.0.CO;2.

Franzke, C. L. E., D. Jelic, S. Lee, and S. B. Feldstein, 2019: Systematic decomposition of the MJO and its Northern Hemispheric extratropical response into Rossby and inertio-gravity components. *Quart. J. Roy. Meteor. Soc.*, **145**, 1147–1164, https://doi.org/10.1002/qj.3484.

Frederiksen, J. S., and C. S. Frederiksen, 1997: Mechanisms of the formation of intraseasonal oscillations and Australian monsoon disturbances: The roles of convection, barotropic and baroclinic instability. *Contrib. Atmos. Phys.*, **70**, 39–56.

Fulton, S. R., and W. H. Schubert, 1985: Vertical normal mode transforms: Theory and application. *Mon. Wea. Rev.*, **113**, 647–658, https://doi.org/10.1175/1520-0493(1985)113<0647:VNMTTA>2.0.CO;2.

Garfinkel, C. I., and D. L. Hartmann, 2011a: The influence of the quasi-biennial oscillation on the troposphere in winter in a hierarchy of models. Part I: Simplified dry GCMs. *J. Atmos. Sci.*, **68**, 1273–1289, https://doi.org/10.1175/2011JAS3665.1.

——, and ——, 2011b: The influence of the quasi-biennial oscillation on the troposphere in winter in a hierarchy of models. Part II: Perpetual winter WACCM runs. *J. Atmos. Sci.*, **68**, 2026–2041, https://doi.org/10.1175/2011JAS3702.1.

Gehne, M., and R. Kleeman, 2012: Spectral analysis of tropical atmospheric dynamical variables using a linear shallow-water modal decomposition. *J. Atmos. Sci.*, **69**, 2300–2316, https://doi.org/10.1175/JAS-D-10-05008.1.

Gill, A. E., 1980: Some simple solutions for heat-induced tropical circulation. *Quart. J. Roy. Meteor. Soc.*, **106**, 447–462, https://doi.org/10.1002/qj.49710644905.

Gray, L. J., J. A. Anstey, Y. Kawatani, H. Lu, S. Osprey, and V. Schenzinger, 2018: Surface impacts of the quasi biennial oscillation. *Atmos. Chem. Phys.*, **18**, 8227–8247, https://doi.org/10.5194/acp-18-8227-2018.

Haertel, P., 2022: Kelvin and Rossby wave contributions to the mechanisms of the Madden-Julian oscillation. *Geosciences*, **12**, 314, https://doi.org/10.3390/geosciences12090314.

Hall, N. M. J., H. H. Le, and S. Leroux, 2020: The extratropical response to a developing MJO: Forecast and climate simulations with the DREAM model. *Climate Dyn.*, **55**, 813–829, https://doi.org/10.1007/s00382-020-05299-y.

Hayashi, M., and H. Itoh, 2017: A new mechanism of the slow eastward propagation of unstable disturbances with convection in the tropics: Implications for the MJO. *J. Atmos. Sci.*, **74**, 3749–3769, https://doi.org/10.1175/JAS-D-16-0300.1.

Hendon, H. H., and M. L. Salby, 1994: The life cycle of the Madden–Julian oscillation. *J. Atmos. Sci.*, **51**, 2225–2237, https://doi.org/10.1175/1520-0469(1994)051<2225:TLCOTM>2.0.CO;2.

Hoskins, B. J., and T. Ambrizzi, 1993: Rossby wave propagation on a realistic longitudinally varying flow. *J. Atmos. Sci.*, **50**, 1661–1671, https://doi.org/10.1175/1520-0469(1993)050<1661:RWPOAR>2.0.CO;2.

——, and G.-Y. Yang, 2000: The equatorial response to higher-latitude forcing. *J. Atmos. Sci.*, **57**, 1197–1213, https://doi.org/10.1175/1520-0469(2000)057<1197:TERTHL>2.0.CO;2.

Hsieh, T.-L., C.-Y. Chang, I. M. Held, and P. Zurita-Gotor, 2021: Nonlinear generation of long waves and the reversal of eddy momentum fluxes in a two-layer quasigeostrophic model. *J. Atmos. Sci.*, **78**, 3525–3536, https://doi.org/10.1175/JAS-D-20-0368.1.

Hsu, H.-H., 1996: Global view of the intraseasonal oscillation during northern winter. *J. Climate*, **9**, 2386–2406, https://doi.org/10.1175/1520-0442(1996)009<2386:GVOTIO>2.0.CO;2.

Jiang, X., and Coauthors, 2020: Fifty years of research on the Madden–Julian oscillation: Recent progress, challenges, and perspectives. *J. Geophys. Res. Atmos.*, **125**, e2019JD030911, https://doi.org/10.1029/2019JD030911.

Jin, F., and B. J. Hoskins, 1995: The direct response to tropical heating in a baroclinic atmosphere. *J. Atmos. Sci.*, **52**, 307–319, https://doi.org/10.1175/1520-0469(1995)052<0307:TDRTTH>2.0.CO;2.

Kasahara, A., 1980: Effect of zonal flows on the free oscillations of a barotropic atmosphere. *J. Atmos. Sci.*, **37**, 917–929, https://doi.org/10.1175/1520-0469(1980)037<0917:EOZFOT>2.0.CO;2.

Kiladis, G. N., and K. M. Weickmann, 1992: Circulation anomalies associated with tropical convection during northern winter. *Mon. Wea. Rev.*, **120**, 1900–1923, https://doi.org/10.1175/1520-0493(1992)120<1900:CAAWTC>2.0.CO;2.

——, K. H. Straub, and P. T. Haertel, 2005: Zonal and vertical structure of the Madden–Julian oscillation. *J. Atmos. Sci.*, **62**, 2790–2809, https://doi.org/10.1175/JAS3520.1.

——, M. C. Wheeler, P. T. Haertel, K. H. Straub, and P. E. Roundy, 2009: Convectively coupled equatorial waves. *Rev. Geophys.*, **47**, RG2003, https://doi.org/10.1029/2008RG000266.

Kim, J.-E., and C. Zhang, 2021: Core dynamics of the MJO. *J. Atmos. Sci.*, **78**, 229–248, https://doi.org/10.1175/JAS-D-20-0193.1.

Kitsios, V., T. J. O'Kane, and N. Žagar, 2019: A reduced-order representation of the Madden–Julian oscillation based on reanalyzed normal mode coherences. *J. Atmos. Sci.*, **76**, 2463–2480, https://doi.org/10.1175/JAS-D-18-0197.1.

Knippertz, P., and Coauthors, 2022: The intricacies of identifying equatorial waves. *Quart. J. Roy. Meteor. Soc.*, **148**, 2814–2852, https://doi.org/10.1002/qj.4338.

Knutson, T. R., and K. M. Weickmann, 1987: 30–60 day atmospheric oscillations: Composite life cycles of convection and circulation anomalies. *Mon. Wea. Rev.*, **115**, 1407–1436, https://doi.org/10.1175/1520-0493(1987)115<1407:DAOCLC>2.0.CO;2.

Kosovelj, K., F. Kucharski, F. Molteni, and N. Žagar, 2019: Modal decomposition of the global response to tropical heating perturbations resembling MJO. *J. Atmos. Sci.*, **76**, 1457–1469, https://doi.org/10.1175/JAS-D-18-0203.1.

Kraucunas, I., and D. L. Hartmann, 2007: Tropical stationary waves in a nonlinear shallow-water model with realistic basic states. *J. Atmos. Sci.*, **64**, 2540–2557, https://doi.org/10.1175/JAS3920.1.

Lau, K.-M., and T. J. Phillips, 1986: Coherent fluctuations of extratropical geopotential height and tropical convection in intraseasonal time scales. *J. Atmos. Sci.*, **43**, 1164–1181, https://doi.org/10.1175/1520-0469(1986)043<1164:CFOFGH>2.0.CO;2.

Lau, N.-C., and K.-M. Lau, 1986: The structure and propagation of intraseasonal oscillations appearing in a GFDL general circulation model. *J. Atmos. Sci.*, **43**, 2023–2047, https://doi.org/10.1175/1520-0469(1986)043<2023:TSAPOI>2.0.CO;2.

Liebmann, B., and D. L. Hartmann, 1984: An observational study of tropical–midlatitude interaction on intraseasonal time scales during winter. *J. Atmos. Sci.*, **41**, 3333–3350, https://doi.org/10.1175/1520-0469(1984)041<3333:AOSOTI>2.0.CO;2.

Lin, H., and G. Brunet, 2011: Impact of the North Atlantic Oscillation on the forecast skill of the Madden-Julian oscillation. *Geophys. Res. Lett.*, **38**, L02802, https://doi.org/10.1029/2010GL046131.

——, ——, and J. Derome, 2007: Intraseasonal variability in a dry atmospheric model. *J. Atmos. Sci.*, **64**, 2422–2441, https://doi.org/10.1175/JAS3955.1.

——, ——, and R. Mo, 2010: Impact of the Madden–Julian oscillation on wintertime precipitation in Canada. *Mon. Wea. Rev.*, **138**, 3822–3839, https://doi.org/10.1175/2010MWR3363.1.

Lin, J.-L., M. Zhang, and B. Mapes, 2005: Zonal momentum budget of the Madden–Julian oscillation: The source and strength of equivalent linear damping. *J. Atmos. Sci.*, **62**, 2172–2188, https://doi.org/10.1175/JAS3471.1.

Ma, D., and Z. Kuang, 2016: A mechanism-denial study on the Madden–Julian oscillation with reduced interference from mean state changes. *Geophys. Res. Lett.*, **43**, 2989–2997, https://doi.org/10.1002/2016GL067702.

Majda, A. J., and J. A. Biello, 2003: The nonlinear interaction of barotropic and equatorial baroclinic Rossby waves. *J. Atmos. Sci.*, **60**, 1809–1821, https://doi.org/10.1175/1520-0469(2003)060<1809:TNIOBA>2.0.CO;2.

Maloney, E. D., and D. L. Hartmann, 1998: Frictional moisture convergence in a composite life cycle of the Madden–Julian oscillation. *J. Climate*, **11**, 2387–2403, https://doi.org/10.1175/1520-0442(1998)011<2387:FMCIAC>2.0.CO;2.

Martin, Z., C. Orbe, S. Wang, and A. Sobel, 2021: The MJO–QBO relationship in a GCM with stratospheric nudging. *J. Climate*, **34**, 4603–4624, https://doi.org/10.1175/JCLI-D-20-0636.1.

Matsuno, T., 1966: Quasi-geostrophic motions in the equatorial area. *J. Meteor. Soc. Japan*, **44**, 25–43, https://doi.org/10.2151/jmsj1965.44.1_25.

Matthews, A. J., B. J. Hoskins, and M. Masutani, 2004: The global response to tropical heating in the Madden–Julian oscillation during the northern winter. *Quart. J. Roy. Meteor. Soc.*, **130**, 1991–2011, https://doi.org/10.1256/qj.02.123.

Monteiro, J. M., A. F. Adames, J. M. Wallace, and J. S. Sukhatme, 2014: Interpreting the upper level structure of the Madden–Julian oscillation. *Geophys. Res. Lett.*, **41**, 9158–9165, https://doi.org/10.1002/2014GL062518.

Moon, W., G. E. Manucharyan, and H. A. Dijkstra, 2022: Baroclinic instability and large-scale wave propagation in a planetary-scale atmosphere. *Quart. J. Roy. Meteor. Soc.*, **148**, 809–825, https://doi.org/10.1002/qj.4232.

Potter, S. F., G. K. Vallis, and J. L. Mitchell, 2014: Spontaneous superrotation and the role of Kelvin waves in an idealized dry GCM. *J. Atmos. Sci.*, **71**, 596–614, https://doi.org/10.1175/JAS-D-13-0150.1.

Ray, P., and C. Zhang, 2010: A case study of the mechanics of extratropical influence on the initiation of the Madden–Julian oscillation. *J. Atmos. Sci.*, **67**, 515–528, https://doi.org/10.1175/2009JAS3059.1.

——, and T. Li, 2013: Relative roles of circumnavigating waves and extratropics on the MJO and its relationship with the mean state. *J. Atmos. Sci.*, **70**, 876–893, https://doi.org/10.1175/JAS-D-12-0153.1.

Rostami, M., and V. Zeitlin, 2019: Eastward-moving convection-enhanced modons in shallow water in the equatorial tangent plane. *Phys. Fluids*, **31**, 021701, https://doi.org/10.1063/1.5080415.

——, and ——, 2020: Can geostrophic adjustment of baroclinic disturbances in the tropical atmosphere explain MJO events? *Quart. J. Roy. Meteor. Soc.*, **146**, 3998–4013, https://doi.org/10.1002/qj.3884.

Rui, H., and B. Wang, 1990: Development characteristics and dynamic structure of tropical intraseasonal convection anomalies. *J. Atmos. Sci.*, **47**, 357–379, https://doi.org/10.1175/1520-0469(1990)047<0357:DCADSO>2.0.CO;2.

Sakaeda, N., and P. E. Roundy, 2014: The role of interactions between multiscale circulations on the observed zonally averaged zonal wind variability associated with the Madden–Julian oscillation. *J. Atmos. Sci.*, **71**, 3816–3836, https://doi.org/10.1175/JAS-D-13-0304.1.

——, and ——, 2015: The development of upper-tropospheric wind over the Western Hemisphere in association with MJO convective initiation. *J. Atmos. Sci.*, **72**, 3138–3160, https://doi.org/10.1175/JAS-D-14-0293.1.

Sardeshmukh, P. D., and B. J. Hoskins, 1988: The generation of global rotational flow by steady idealized tropical divergence. *J. Atmos. Sci.*, **45**, 1228–1251, https://doi.org/10.1175/1520-0469(1988)045<1228:TGOGRF>2.0.CO;2.

Schwendike, J., G. J. Berry, K. Fodor, and M. J. Reeder, 2021: On the relationship between the Madden–Julian oscillation and the Hadley and Walker circulations. *J. Geophys. Res. Atmos.*, **126**, e2019JD032117, https://doi.org/10.1029/2019JD032117.

Seo, K.-H., and H.-J. Lee, 2017: Mechanisms for a PNA-like teleconnection pattern in response to the MJO. *J. Atmos. Sci.*, **74**, 1767–1781, https://doi.org/10.1175/JAS-D-16-0343.1.

Showman, A. P., and L. M. Polvani, 2011: Equatorial superrotation on tidally locked exoplanets. *Astrophys. J.*, **738**, 71, https://doi.org/10.1088/0004-637X/738/1/71.

Sobel, A. H., J. Nilsson, and L. M. Polvani, 2001: The weak temperature gradient approximation and balanced tropical moisture waves. *J. Atmos. Sci.*, **58**, 3650–3665, https://doi.org/10.1175/1520-0469(2001)058<3650:TWTGAA>2.0.CO;2.

Stone, P. H., and J. H. Carlson, 1979: Atmospheric lapse rate regimes and their parameterization. *J. Atmos. Sci.*, **36**, 415–423, https://doi.org/10.1175/1520-0469(1979)036<0415:ALRRAT>2.0.CO;2.

Straus, D. M., and R. S. Lindzen, 2000: Planetary-scale baroclinic instability and the MJO. *J. Atmos. Sci.*, **57**, 3609–3626, https://doi.org/10.1175/1520-0469(2000)057<3609:PSBIAT>2.0.CO;2.

Tseng, K.-C., E. Maloney, and E. Barnes, 2019: The consistency of MJO teleconnection patterns: An explanation using linear Rossby wave theory. *J. Climate*, **32**, 531–548, https://doi.org/10.1175/JCLI-D-18-0211.1.

Tulich, S. N., and G. N. Kiladis, 2021: On the regionality of moist Kelvin waves and the MJO: The critical role of the background zonal flow. *J. Adv. Model. Earth Syst.*, **13**, e2021MS002528, https://doi.org/10.1029/2021MS002528.

Wang, B., and H. Rui, 1990: Dynamics of the coupled moist Kelvin–Rossby wave on an equatorial β-plane. *J. Atmos. Sci.*, **47**, 397–413, https://doi.org/10.1175/1520-0469(1990)047<0397:DOTCMK>2.0.CO;2.

——, and X. Xie, 1996: Low-frequency equatorial waves in vertically sheared zonal flow. Part I: Stable waves. *J. Atmos. Sci.*, **53**, 449–467, https://doi.org/10.1175/1520-0469(1996)053<0449:LFEWIV>2.0.CO;2.

Wedi, N. P., and P. K. Smolarkiewicz, 2010: A nonlinear perspective on the dynamics of the MJO: Idealized large-eddy

simulations. *J. Atmos. Sci.*, **67**, 1202–1217, https://doi.org/10.1175/2009JAS3160.1.

Weickmann, K. M., G. R. Lussky, and J. E. Kutzbach, 1985: Intraseasonal (30–60 day) fluctuations of outgoing longwave radiation and 250 mb streamfunction during northern winter. *Mon. Wea. Rev.*, **113**, 941–961, https://doi.org/10.1175/1520-0493(1985)113<0941:IDFOOL>2.0.CO;2.

Wolding, B. O., E. D. Maloney, S. Henderson, and M. Branson, 2017: Climate change and the Madden–Julian oscillation: A vertically resolved weak temperature gradient analysis. *J. Adv. Model. Earth Syst.*, **9**, 307–331, https://doi.org/10.1002/2016MS000843.

Xu, K.-M., and K. A. Emanuel, 1989: Is the tropical atmosphere conditionally unstable? *Mon. Wea. Rev.*, **117**, 1471–1479, https://doi.org/10.1175/1520-0493(1989)117<1471:ITTACU>2.0.CO;2.

Yang, G.-Y., B. Hoskins, and J. Slingo, 2003: Convectively coupled equatorial waves: A new methodology for identifying wave structures in observational data. *J. Atmos. Sci.*, **60**, 1637–1654, https://doi.org/10.1175/1520-0469(2003)060<1637:CCEWAN>2.0.CO;2.

Yano, J.-I., and J. J. Tribbia, 2017: Tropical atmospheric Madden–Julian oscillation: A strongly nonlinear free solitary Rossby wave? *J. Atmos. Sci.*, **74**, 3473–3489, https://doi.org/10.1175/JAS-D-16-0319.1.

Žagar, N., and C. L. E. Franzke, 2015: Systematic decomposition of the Madden-Julian oscillation into balanced and inertio-gravity components. *Geophys. Res. Lett.*, **42**, 6829–6835, https://doi.org/10.1002/2015GL065130.

——, A. Kasahara, K. Terasaki, J. Tribbia, and H. Tanaka, 2015: Normal-mode function representation of global 3-D data sets: Open-access software for the atmospheric research community. *Geosci. Model Dev.*, **8**, 1169–1195, https://doi.org/10.5194/gmd-8-1169-2015.

——, F. Lunkeit, F. Sielmann, and W. Xiao, 2022: Three-dimensional structure of the equatorial Kelvin wave: Vertical structure functions, equivalent depths, and frequency and wavenumber spectra. *J. Climate*, **35**, 2209–2230, https://doi.org/10.1175/JCLI-D-21-0342.1.

Zhang, C., and P. J. Webster, 1992: Laterally forced equatorial perturbations in a linear model. Part I: Stationary transient forcing. *J. Atmos. Sci.*, **49**, 585–607, https://doi.org/10.1175/1520-0469(1992)049<0585:LFEPIA>2.0.CO;2.

——, Á. F. Adames, B. Khouider, B. Wang, and D. Yang, 2020: Four theories of the Madden–Julian oscillation. *Rev. Geophys.*, **58**, e2019RG000685, https://doi.org/10.1029/2019RG000685.

Zurita-Gotor, P., and I. M. Held, 2018: The finite-amplitude evolution of mixed Kelvin–Rossby wave instability and equatorial superrotation in a shallow-water model and an idealized GCM. *J. Atmos. Sci.*, **75**, 2299–2316, https://doi.org/10.1175/JAS-D-17-0386.1.